DOI: https://doi.org/10.2138/am-2018-6290

REVISION # 2

Mapping the distribution of melt during anatexis at the source area of crustal granites by synchrotron μ-XRF

Fabio Ferri[1,2*], Antonio Acosta-Vigil[2,3,4], Carlos Alberto Perez[5] and Nicolás Hayek[1]

(1) Universidad de los Andes, Bogotá, Colombia,

(2) Universitá degli Studi di Padova, Padua, Italy,

(3) The Australian National University, Canberra, Australia,

(4) Instituto Andaluz de Ciencias de la Tierra, CSIC-Universidad de Granada, Spain,

(5) LNLS, Laboratório Nacional de Luz Sincrotron, Campinas, Brazil

[*] Corresponding author. Tel: +39-049-8279197; Fax: +39-049-8272010.

E-mail addresses: fabio.ferri@unipd.it

Abstract

The garnet-biotite-sillimanite enclaves from El Hoyazo are quenched anatectic metapelites found within peraluminous dacites (Betic Cordillera, SE Spain), representing a residual lower crust in the area after 40-60 % of melt extraction. Anatexis occurred concomitantly with deformation in a regional metamorphic setting during the Upper Miocene at the base of the continental crust. Previous studies have provided detailed information on the pressure-temperature evolution, sequence of melting reactions and associated melt proportions and compositions. They show that enclaves mostly record peak metamorphic assemblages, mineral compositions and, likely, microstructures, with minor changes upon entrapment within the dacite magma and rapid ascent and extrusion. The enclaves still preserve a proportion of the primary melt, that solidified to glass in abundant melt inclusions (MI) and matrix melt, permitting the study of the microstructural relationships between melt and residue. This study focuses on the geometry of the glass network at the micro-scale which, combined with the previously reported anatectic history, helps shed light on the mechanisms and history of melt drainage from these rocks.

A representative sample of the enclaves was investigated by synchrotron μ-XRF and Scanning Electron Microscopy to map the distribution of glass and minerals on three thin sections cut perpendicularly to the foliation. The combination of major and trace element μ-XRF distribution maps and detailed backscattered electron images evidence the presence of a pervasive and mostly interconnected glass network through the studied centimeter-scale sections. Interconnection is due to the crosscutting of films and glass-rich domains oriented parallel and at high angle with foliation. Although enclaves lost ≈40-60 % of melt, they still contain ≈10-15 % of glass, with a considerable proportion of it stored within the Mix – an aggregate of micron-sized fibrolitic sillimanite and glass. The distribution of glass (former

43 melt) is not in textural equilibrium with the solid residue, and resembles the interconnected
44 network of deformation bands observed in migmatites of anatectic terranes at the meso-scale.
45 Microstructural studies of melt pseudomorphs in migmatites and granulites of anatectic
46 terranes are scarce, but the following remarkable interpretations can be made combining our
47 observations of these enclaves: melt formed an interconnected network during anatexis that
48 permitted melt segregation and extraction, though melt-residue textural disequilibrium is the
49 rule rather than the exception. The proportion of melt present in residual migmatites can be
50 much higher than the permeability threshold for crustal protoliths; in this particular study, two
51 reasons for this might be that (i) melt was still being produced and flowing through the
52 residual migmatite right before disaggregation and inclusion within the host dacite, where
53 additional melt drainage was impeded by the hydrostatic stress field, and (ii) a particular
54 microstructure produced at the onset of anatexis, such as the Mix, acted as a trap for melt
55 impeding or delaying melt segregation.

56 **1. Introduction**

57 The extraction of granitic magma *sensu lato* from middle to lower anatectic continental
58 crust and its ascent and intrusion into the upper crust to form granitoid plutons, or extrusion to
59 form volcanic deposits, is the principal process by which continents differentiate into a more
60 mafic deep portion and a more felsic shallow domain, and represents the most important mass
61 transfer mechanism affecting the continental crust (Brown et al., 2011, and references
62 therein). The magmas feeding these high-level plutons and volcanic deposits may contain
63 variable proportions of minerals from their source areas (Chappell et al. 1987; Stevens et al.
64 2007; Garcia-Arias and Stevens 2016), and partially crystallize and differentiate upon
65 extraction and ascent (Morfin et al. 2014; Brown et al. 2016; Carvalho et al. 2016).
66 Nevertheless, the genesis of such magmas requires crustal melts to largely segregate from the
67 solid residue at their source areas in the lower crust, and move along some kind of network

that eventually feeds these intrusions or volcanic deposits. Segregation of the melt from its residue in the anatectic terrane by melt flow and/or mass flow along grain boundaries and fractures (e.g. Marchildon and Brown 2002) is the first step in this process, and knowing its mechanisms and timing is important to gain information about (i) its control on the composition of the extracted melt and magma, (ii) the extent of equilibration between extracted melt and residue and, upon magma extraction and ascent, (iii) its role on crustal differentiation. Understanding melt segregation starts by recognizing the geometry of this grain-scale melt drainage network at the source area (Sawyer 2001).

Theoretical considerations and experimental observations indicate that, under textural equilibrium conditions, granitoid melts produced during the anatexis of crustal rocks reach interconnection throughout the solid residue at very low degrees of melting (<1 to a few volume % of melt: Laporte and Watson 1995; Laporte et al. 1997; Rosenberg and Handy 2005; Holness 2006). This fact, coupled with (i) the realization about the importance of pressure gradients produced by tectonic stress and heterogeneous deformation of the anatectic crust on melt migration, (ii) field observations that regional anatexis is systematically accompanied by stress and deformation (McLellan 1988; Sawyer 1994, 2008; Brown et al. 1995; Rutter and Neumann 1995; Brown and Solar 1998), as well as with (iii) several geochemical studies showing that leucosomes are frequently undersaturated in trace elements controlled by the dissolution of accessory minerals (e.g. Barbey et al. 1989; Sawyer 1991), have led to the general consensus that anatectic melts can be rapidly segregated from the residue and extracted from the anatectic terrane (Brown et al. 1995, 2011).

The main evidence for crustal melting and melt segregation and extraction from the lower levels of the continental crust comes from petrological and geochemical studies of exhumed regional-scale migmatite-granite complexes. In general, the geometry and orientation of the melt drainage network is controlled by the distribution of fertile layers and minimum melting

93 assemblages, by fabrics and location of low-pressure sites formed during differential stress
94 affecting heterogeneous rocks, and by the nature and orientation of the strain field (e.g.
95 Brown et al. 1995; Collins and Sawyer 1996; Olivier and Barr 1997; Brown and Solar 1999;
96 Solar and Brown 2001; Sawyer 2001; Guernina and Sawyer 2003; Brown 2004, 2007; White
97 et al. 2004; Brown et al. 2011; Závada et al., 2007). At the mesoscale, this drainage network
98 is more evident and manifested as interconnected leucosomes (and/or their associated
99 melanosomes) and discordant granitic veins and dikes; these structures collect the melt
100 produced in the adjacent partially melted domains, and transfer it out of the anatectic region
101 (Brown 1994, 2007; Sawyer 2001, 2014; Brown et al. 1999; Guernina and Sawyer 2003;
102 Marchildon and Brown 2003). At the grain-scale, however, the network connecting partially
103 melted domains being drained and macroscopic leucosomes is not evident. This is mostly
104 because (i) anatexis in regional metamorphic terranes is accompanied by deformation, and
105 melt is thought to mostly segregate and migrate from the residue, remaining only in very
106 small proportions at the site of generation; and (ii) any former intergranular melt present
107 above the solidus may have reacted back with the residue and crystallized during the slow
108 cooling at depth. As a consequence, the geometry of the grain-scale melt paths during the
109 early stages of segregation remains one of the least known parts of the melt segregation and
110 extraction process (Sawyer 2001, 2014).
111 The investigation of this topic has been approached through detailed microstructural
112 studies of melt pseudomorphs (Harte et al. 1993; Clemens and Holness 2000) in a limited
113 number of residual anatectic terranes (Sawyer 2001, 2014; Marchildon and Brown 2002;
114 Holness and Sawyer 2008). These studies indicate that the inferred distribution of melt is not
115 in textural equilibrium with the solid residue, mostly because textural equilibration was not
116 achieved during anatexis, even if the investigated residual anatectic rocks show that a large
117 proportion of melt (≈15-35%) was extracted during partial melting. Thus former melt appears

mostly as thin films along many of the grain boundaries (including frequently two-grain junctions), a few to a few tens of μm in thickness, one to several grain diameters in length, and variable degrees of interconnection depending on melt proportion. More rarely, it also occurs as pools hundreds of μm in size. Melt commonly appears in between reactant minerals, with an orientation controlled by the rock fabric, a proportion that varies at the mm-cm scale between ≈2-6, 12 or even 20-25 vol.%, and associated dihedral angles grouped within two or more populations, commonly ≈10-30°, 60-80° and 80-100°.

In the present study we report the X-ray grain-scale mapping of the intergranular melt network in one sample of very particular migmatites, the foliated and residual anatectic metasedimentary enclaves hosted by peraluminous dacites at El Hoyazo, SE Spain. Detailed petrological and geochemical studies have concluded that these rocks are mostly equilibrated at the peak anatectic conditions, and that most of the anatectic history recorded in them took place in a regional syn-deformation environment (Cesare 2008; Acosta-Vigil et al. 2010). The process of regional anatexis was frozen due to apparently minor modifications of the studied enclaves after incorporation into the dacite magma, and quenching upon rapid ascent and extrusion. Melt present during anatexis solidified to glass and hence the rocks are ideal to investigate the distribution and segregation of melt during crustal anatexis at or near peak conditions. This contrasts with anatectic terranes whose inferred melt distributions might record variable stages of the process of melt production and segregation, and that may have been modified by melt-residue back reaction, melt crystallization and subsolidus equilibration. The melt network mapped within the studied sample is compared with intergranular melt distributions described from previous studies of anatectic terranes. This, in addition to providing information on the geometry of the grain-scale melt pathways during segregation at peak conditions, may also help to assess the nature of the information provided by melt pseudomorphs in anatectic terranes. Eventually, it also might help understanding the

143 relationships between grain-scale and mesoscale melt distributions in anatectic complexes.

144 **2. Sample description**

145 **2.1 Geological setting**

146 The studied sample is a metapelitic enclave collected from the dacitic lava of El Hoyazo, a
147 volcanic centre located in the Neogene Volcanic Province (NVP) of SE Spain, in the Betic
148 Cordillera (Fig. 1; Lopez Ruiz and Rodriguez Badiola 1980). The dome comprises strongly
149 peraluminous cordierite-bearing dacites, which host abundant enclaves (~20-25 vol.%) of
150 predominantly anatectic metapelites (~10-15 vol.%) classified into three main petrographic
151 groups: Grt-Bt-Sil, Spl-Crd and Qz-Crd rocks (Zeck 1970,1992) (abbreviations after Whitney
152 and Evans 2010). Garnet-Bt-Sil enclaves are predominant at El Hoyazo, and the
153 representative Grt-Bt-Sil enclave HO1 was selected for mapping the distribution of glass.
154 HO1 was previously used as well in the experimental investigation of Ferri et al. (2007)
155 aiming at measuring the P-waves seismic velocities of pelitic lower continental crust up to
156 conditions of partial melting.

157 Garnet-Bt-Sil enclaves are foliated, medium- to coarse-grained granulite-facies rocks, that
158 preserve abundant fresh leucogranitic glass (quenched melt, hereafter "glass") as both primary
159 MI in most minerals and along grain boundaries (Cesare et al. 1997; Acosta-Vigil et al. 2007).
160 The melt was produced by anatexis of the metasedimentary protolith and did not infiltrate
161 from the enclosing dacite (Cesare et al. 1997; Acosta-Vigil et al. 2010). Together with a
162 residual bulk-rock geochemistry, this is evidence of partial melting and melt extraction
163 (Cesare et al. 1997; Cesare and Maineri 1999; Cesare and Gómez-Pugnaire 2001).

164 The estimated peak conditions of anatexis for the Grt-Bt-Sil enclaves at El Hoyazo are
165 ≈850 ± 50°C and 0.5–0.7 GPa (Cesare et al. 1997; Cesare and Gómez -Pugnaire 2001),
166 implying partial melting at ≈20 km depth (assuming a crustal density of ~ 2.7 g cm^{-3}), a value
167 which approximates the depth of the actual Moho in the area (~ 21 km, Torne et al. 2000). U-

Pb dating of MI-bearing zircons and monazites (Cesare et al. 2003b, 2009) indicates an age for anatexis (metamorphic peak) of 9.3-9.9 Ma, whereas the host dacite extruded at 6.3 Ma (Zeck and Williams 2002), suggesting melt residence times of ≈3 Ma at the source area (Cesare et al. 2003b). Similar anatectic enclaves are abundant in dacites outcropping throughout the ≈200-km long volcanic belt constituting the NVP (Cesare and Gómez - Pugnaire 2001; Álvarez-Valero and Kriegsman 2007, 2008). Hence the studied Grt–Bt–Sil enclave may be considered as an analogue of the deep anatectic crust beneath the El Hoyazo volcano in the late Miocene. These observations constitute also a first indication that anatexis of the enclaves was likely not a consequence of their incorporation into the dacite magma, but occurred in a regional setting (see below).

2.2 Bulk rock composition, petrography and anatectic history

The bulk composition of sample HO1 is reported in Table 1. It is very low in SiO_2 (≈45 wt.%) and high in Al_2O_3 (≈32 wt.%) and Fe_2O_3 (≈11 wt.%), with a C content up to ≈1 wt.%. The composition is similar to other Grt-Bt-Sil enclaves from El Hoyazo (e.g., Cesare et al. 1997; Acosta-Vigil et al. 2010, Cesare and Acosta-Vigil 2011), and their extreme residual character is consistent with high degrees of extraction of a granite melt component. Geochemical work by Acosta-Vigil et al. (2010) determined that more than 60% cumulative melt should have been produced during the prograde P-T evolution of these enclaves (see below), whereas mass balance calculations by Cesare et al. (1997) indicate ≈40–60 wt.% of this melt was extracted.

The enclave is made of garnet, biotite, sillimanite, plagioclase, glass, graphite and minor ilmenite and hercynite. Accessory minerals include apatite, zircon and monazite. Quartz is absent. The rock is medium-grained and displays a well-developed foliation defined by biotite–sillimanite rich layers and oriented graphite (Fig. 2). Most sillimanite is fibrolitic, appears intimately intergrown with rhyolitic melt (hereafter called the “Mix” after Cesare et

al. 1997), and was apparently produced by Ms breakdown-melting reactions (Cesare and Gomez-Pugnaire, 2001). Locally, the Mix is in rounded knots apparently pseudomorphosing porphyroblasts such as garnet. The foliation anastomoses around garnet porphyroblasts (up to 8 mm diameter) and the Mix knots. The plagioclase is elongated parallel to the foliation. Glass is abundant, both as primary MI in all minerals (particularly in garnet and plagioclase) and in the matrix, e.g. constituting part of the Mix or locally intermixed with plagioclase, or in tens to hundred of μm–thick films parallel to the foliation, as coatings around garnets, or in pockets located in strain shadows around porphyroblasts.

According to Cesare et al. (1997) and Acosta-Vigil et al. (2010), the abundance of Bt and Sil may be explained because either (i) these phases were already present in the lower-grade protolith and/or (ii) they were produced, together with H_2O, during rapid heating by dehydration reactions involving Ms, Chl, Grt, St and Qz (e.g. Yardley 1989). The presence of MI in all minerals, including common reactants in crustal melting reactions e.g. Pl, supports rapid melting of a low-grade protolith and crystallization of high grade assemblages, by-passing melting reactions (Cesare and Maineri 1999). The large amount of melt produced by anatexis of these enclaves, as well as the presence of quite a large amount of Bt is in accordance with H_2O having remained sequestered in the system by rapid incorporation into the melt during rapid heating and melting. The presence of Sil + melt intergrowths (the "Mix") strongly suggests the occurrence of a peritectic melting reaction involving Ms + Pl + Qz (Acosta-Vigil et al. 2010).

A considerable number of detailed petrological and geochemical studies have concluded that melt was mostly produced in a regional setting in the presence of stress and deformation, by the following reactions along the prograde path until reaching peak conditions (see section 5.2 for details): (i) H_2O-rich fluid-present melting of Ms at ≈700 ºC producing ≈15-20 wt.% of melt, whose remains are represented now as MI in Pl; (ii) fluid-absent breakdown-melting

of muscovite at ≈750 ºC producing ≈15-25 wt.% of melt, registered now as MI in Grt; and (iii) the beginning of the fluid-absent breakdown-melting of biotite starting at ≈800 ºC, ending at peak conditions and producing ≈15 wt.% of melt, manifested as glass films in the matrix (Acosta-Vigil et al. 2010). There are several arguments supporting that most of the anatectic history of these enclaves occurred in a regional setting, and that enclaves only experienced minor modifications after entrapment into the dacite magma, ascent, extrusion and quenching. Peak metamorphic conditions, using Grt, Pl and Bt either wrapped by or defining the main foliation, indicate melting at the base of the continental crust of the area (850±50 ºC, 0.5-0.7 GPa; Cesare et al. 1997). Melt inclusions, representing the remains of about ≈45 wt.% of melt produced by the breakdown-melting of muscovite, are present within Grt and Pl which are wrapped within or aligned along the main foliation of the rock (Cesare et al. 1997; Cesare and Gómez-Pugnaire 2001). Matrix melt commonly forms films parallel to the main foliation or is present in strain shadows of porphyroblast and intermixed with other phases mostly sillimanite (Mix) and plagioclase (Cesare et al. 1997; Cesare and Gómez-Pugnaire 2001). During incorporation into the dacite and decompression, the enclaves presumably stagnated in a shallow magma chamber for $< 10^3$–10^4 years (Alvarez-Valero et al. 2007) and partially equilibrated at ≈820 ± 50°C and ≈0.5 GPa (Alvarez-Valero et al. 2007; Tajcmanová et al. 2009). The rapid ascent caused the fast cooling of rocks and melt, preventing the crystallization of the melt entrained within inclusions and in the matrix, that was quenched to glass.

2.3 Mineral and glass chemistry.

The compositions of minerals of the enclave HO1 (Table 2) are very homogeneous and similar to that of other Grt-Bt-Sil El Hoyazo enclaves reported by Cesare et al. (1997, 2003a, 2003b, 2005) and Acosta-Vigil et al. (2010). Biotite has X_{Fe} = 0.62-0.67 and TiO_2 ~ 5.0 wt.%. Garnet is weakly zoned within the ranges $Alm_{78\text{-}81}Pyp_{10\text{-}14}Sps_{1\text{-}7}Grs_{2\text{-}10}$. Plagioclase is a low-

243 Ca andesine (An_{30-33}).

244 Despite slight compositional variations among MI and interstitial glass (Acosta-Vigil et al.
245 2007 and 2010), glass in Grt-Bt-Sil enclaves is leucogranitic ($FeO + MgO + TiO_2 < 1.65$
246 wt.%), peraluminous ($Al_2O_3/(CaO + Na_2O + K_2O) > 1.11$) and hydrous. Mean H_2O
247 concentration, calculated by the difference of the electron microprobe totals from 100%
248 (Morgan and London, 1996), is around 3-4 wt.% (Acosta-Vigil at el. 2007). Mean wt.%
249 normative compositions plot in the vicinity of the H_2O-undersaturated (a_{H2O}=0.1–0.4)
250 haplogranite eutectics (Acosta-Vigil et al. 2010).

251 The minerals have also characteristic minor and trace element concentrations (Acosta-
252 Vigil et al. 2010), which can help, together with the major elements, the identification of
253 phases from the combination of different XRF chemical maps (see below). For instance, the
254 glass controls the majority of B, As and Cs of the enclave. Biotite hosts a large amount of Cs,
255 Ba, Nb, Ta and most of the Rb, V, Cr, Co, Ni and Zn. Garnet concentrates Sc, Dy, Ho and
256 most of the Y and HREE. Plagioclase show high concentrations of Li, Be, Pb and hosts most
257 of the Sr and Eu, while the scarce residual K-feldspar controls Ba, Pb and part of the Rb, Sr
258 and Eu. Cordierite, when present, concentrates most of the Be.

259 **3. Analytical methods**

260 The distribution of glass within sample HO1 was determined at the X-ray
261 microfluorescence station available at the D09B XRF Fluorescence beamline of the Brazilian
262 Synchrotron Light Laboratory (LNLS) in Campinas, Brazil (Perez et al. 1999), using an X-ray
263 optic based on a pair of dynamically figured mirrors in a so-called KB mirror arrangement.
264 The microfocusing system, fabricated by the X-ray optic group (Zhang et al. 1998) of the
265 European Synchrotron Radiation Facility (ESRF) in France, is able to produce an X-ray
266 microbeam of ≈12 μm × 22 μm in size. Measurements were performed under room
267 temperature and atmospheric pressure conditions. An iron (Fe) filter was placed in front of the

incoming beam in order to reduce distortion of the XRF spectra due to the high X-ray fluorescence intensity contribution of the Fe-K lines coming from the sample matrix. Samples were put in the focus plane within an accuracy of 1 μ with precise remote-controlled motorized stages. An optical microscope (~ 500x magnification) was used to precisely locate the irradiated area. 2D-XRF mapping was tested with different combinations of beam size, step and counting time to get the best compromise between spatial resolution and signal intensity. All maps were acquired at 22 μm diameter beam, 40 μm steps and 0.3 sec counting time, with the exception of a high-resolution map acquired at 25 μm steps and 1.0 sec counting time. Elemental composition per pixel was determined at a standard geometry (45–45°) using a silicon drift detector (KETEK GmbH) with a resolution of 140 eV (FWHM) at 5.9 keV. Spectra processing and elemental imaging reconstructions were done with the PyMca software (Solé et al. 2007), an advanced fitting program developed by the ESRF.

Detailed BSE images of the studied samples were acquired in a variety of specific microstructural locations, using the Scanning Electron Microscopes (SEM) of the Universidad de los Andes in Bogotá and the Universita' di Padova.

The major element composition of the glass throughout the sample was measured using a Cameca SX-50 electron microprobe (EMP) at the University of Oklahoma. Analyses were conducted on areas previously studied by SEM at the Universita' di Padova and the Universidad de Granada. To avoid or minimize alkali loss and changes in major elemental ratios, analytical conditions were used as recommended by Morgan and London (1996, 2005), with a 5 μm spot size and conducting analyses of secondary glass standards during the same analytical session.

3.1 Samples analyzed by μ-XRF

Due to experimental time limitations, it was not possible to perform a three-dimensional μ–XRF tomography; instead the investigation was performed on several thin sections oriented

293 perpendicular according to the axes X, Y and Z of Fig. 3, where the XY plane is parallel to
294 the biotite – graphite foliation, and Z is normal to the foliation. The axis X is along a weak
295 lineation marked by plagioclase and sillimanite crystals. The thin sections were derived from
296 rock volumes adjacent but not directly in contact with each other, as schematically reported in
297 Fig. 3. The thin section (1) HO1YZ is parallel to the YZ plane. Thin sections (2) and (3),
298 HO1XZ and HO1XZexp respectively, are parallel to the XZ plane; thin section HO1XZexp
299 was derived from a core used in the experiments conducted by Ferri et al. (2007), in a position
300 close to that of sections (1) and (2). Section (4) corresponds to a detail area of thin section (1),
301 measured at high resolution with shorter step distance and longer counting time (see details
302 above). The investigated areas were 10 mm x 20 mm for section (1), 9 mm x 9 mm for
303 sections (2) and (3), and 3 mm x 3 mm for section (4).
304 Thin section HO1XZexp was derived from an experimentally treated HO1 sample which
305 was re-heated at 0.5 GPa up to 700°C, under hydrostatic conditions in a gas pressure vessel,
306 in order to measure the change in P-wave velocity with pressure and temperature (Ferri et al.
307 2007). These authors showed that, after the experiment, the volume of the enclave was
308 reduced without any sign of phase reactions, i.e. without affecting the original mineral
309 assemblage. Even though the authors did not characterize the fraction or nature of porosity
310 during the experiment, they inferred a porosity reduction after the experiment, as indicated by
311 a decrease in volume of the sample measured at ambient pressure with a Helium pycnometer.
312 In order to determine such volume variations, samples were heated in steps, and then
313 extracted and measured at progressively increasing temperatures of 400°C, 600°C, 650°C and
314 700°C. The volume reduction was almost linear from room temperature to 600°C, with a
315 porosity reduction of ca. ~ 2.0-2.5% at 600°C, and of 0.5 % from 600°C to 700°C
316 corresponding to a density increase from 2.96 g/cm^3 in the starting material to 3.01 g/cm^3
317 after the experiment (see Fig. 6 in Ferri et al. 2007). Since neither mineral reactions nor glass

crystallization were observed to occur up to 700°C, this volume reduction was attributed to partial closure of pores and microfractures produced by relaxation of interstitial glass. The experiment was performed at P-T conditions below the liquidus (≈800-850 ºC; Holtz et al. 2001) but above the glass transition temperature (≈450 ºC; Giordano et al. 2008) estimated for the mean composition of the matrix glass, and hence glass behaved as a liquid during the experiment. The calculated high viscosities for that melt (≈10^8 Pa s; Giordano et al. 2008) and the hydrostatic conditions of the experiment, however, likely prevented the melt from flowing during the short ≈3-hour experiment, and hence the glass distribution was not modified with respect to the natural rock. Distributions of glass obtained from HO1YZexp (re-heated) and HO1YZ (not re-heated) are quite similar (see below).

4. Results

4.1 Melt distribution

The major and trace element abundances collected during the μ-XRF mapping were combined by means of the RGB Correlator tool of PyMca (Solé et al. 2007), in order to obtain 2D distribution maps of phases in the four thin sections of the studied migmatite. Fig. 4 reports an example of the data processing performed on thin section (4) of Fig. 3. The Fig. 4A was obtained by the RGB combination of signals from Si (red), K (green) and Fe (blue). Biotite is light blue due to the high concentration of Fe and K; the Mix is vermilion due to the abundance of Si; the glass is orange due to the combination of Si, K and Fe. The software ENVI® was used to discriminate the phases by selecting the region of interest (ROI) corresponding to every phase. The μ-XRF spectra were averaged over a large number of pixels (> 10.000), to reduce the variability caused by decay of the beam intensity or mixed analyses. Six ROIs were defined corresponding to the phases biotite, garnet, plagioclase, K-feldspar, glass and the Mix (Figs. 4B and 5B). In order to identify the distribution of Spl and

Ilm in the thin section, a second triplet was analyzed by the RGB combination of signals from Mn (red), Ti (green) and Zn (blue). Due to the limited amount of Spl and Ilm in the thin sections (<0.1 – 0.4 area %) and their small average grain size (< 20–40 μm), however, their distribution could not be included in the images Figs. 4 and 5. Also, the peak of carbon could not be identified from the XRF model profiles defined with the PyMca software, thus the areal distribution of graphite could not be mapped either.

Depending on the size of the glass regions, a major limitation of the RGB maps regarding the studied problem could be the spatial resolution, which is defined by the beam size, 22 μm. In the large mapped areas (sections 1-3; using a beam diameter of 22 μm and 40 μm steps), this may result in mixed analyses of glass+minerals, or even glass might go unnoticed, if glass is present as ≤ 20-30 μm-thick films at the contact between minerals, or when the glass is intimately intergrown with fibrolitic sillimanite as in the Mix. This means that, in areas where glass is ≤ 20-30 μm across, results might show a fuzzy image of the distribution of glass and the proportions of detected glass will likely correspond to minimum values. We evaluated this potential problem in two ways: (i) mapping a small part of section 1 (=section 4; Fig. 3) conducting more closely spaced analyses (beam diameter of 22 μm, 25 μm steps); (ii) conducting SEM-BSE imaging of particular areas of the investigated sections (see below). Nevertheless this technique should provide a reasonable first-order approach to the microscopic distribution of melt in the studied migmatite.

On the basis of the obtained trace element distributions, sillimanite seems to systematically show high concentrations of Gallium (Fig. 4C). The combination of the Gallium concentration map (= sillimanite distribution) with the glass distribution obtained from the Si-K-Fe chemical maps (black areas in Fig. 4B) yields the image of Fig. 4D which evidences that, in this particular area, most of the glass is concentrated within the Mix at the contact with biotite crystals. This procedure was applied to all thin sections and results are reported in

Fig. 5, where the Gallium concentration map is not reported separately as in Fig. 4C but directly overlapped to the Fig. 5B, showing the spatial distribution of the phases of Fig. 5C.

Despite the absence of a 3D tomography of the distribution of melt, and even if we have not studied a section subparallel to foliation, results indicate that glass seems to form a pervasive and mostly interconnected network made of melt films and pools, together with melt-rich domains (intermixture with sillimanite as in the Mix, or with plagioclase) throughout the cm-scale studied volume. This is due mostly to the crosscutting of melt films and melt-rich domains oriented parallel and at a high angle with foliation. Despite the presence of ≈1-5 mm Bt and Mix domains subparallel to foliation, and Grt and Pl porphyroblast, all of which tend to make melt paths more tortuous or irregular, matrix melt seems largely interconnected. They also invade to some extent the Bt domains. It is difficult to precisely estimate the thickness of melt films and melt-rich domains (see above), but in most cases they are probably ≤ 100 μm (Fig. 6B-D); melt pools are ≈0.1-1 mm across (Fig. 6E,F). Distances between melt domains vary between ≈0.25-2 mm. Melt films wet most of the grain boundaries; those oriented parallel to foliation are thinner than those perpendicular or at high angle to the foliation (Fig. 6C, E, F).. We do not observe any main channel (in terms of size) into which smaller channels drain the melt, at least at the scale of several cm and in the studied rock volume, but in general a pervasive and mostly interconnected grain-scale melt network.

Although sample HO1-XZexp –section (3), Fig. 3– was reheated up to 700 ºC at 0.5 GPa (Ferri et al. 2007), its glass distribution looks similar to that observed in HO1-XZ and HO1-YZ (see also section 3.1). The absence of garnet and plagioclase in HO1-XZexp is due to some small-scale mineralogical variability in Grt-Bt-Sil enclaves.

The grain-scale melt network in this migmatite seems to be mostly controlled by syn-anatectic deformation and the orientation of the main foliation, which is largely marked by the

alignment of biotite. However, it is also controlled to some extent by metamorphic microstructures, such as the shape and distribution of the Mix (sometimes this Sil+glass aggregate does not follow but truncates the main foliation, and melt films anastomose around it) and the nature of the Mix (see section 5.2). For the same reason, in rock domains where garnet and plagioclase are particularly abundant, as in section HO1-XZ, the glass network becomes more irregular as it anastomoses around porphyroblasts of these minerals.

The correspondence between the phase distributions reported in Figs. 4 and 5 using μ-XRF mapping, and the petrography of the studied sample, was verified on detailed SEM-BSE images acquired in specific microstructural positions of the studied thin sections (Figs. 6 and 7). The SEM analysis confirms that glass forms either thin films or pools in between most of the minerals, e.g. plagioclase and garnet (Fig. 6A), plagioclase and biotite (Figs. 6B), garnet and biotite (Figs. 6D, F and 7B), biotite and the Mix (Fig. 6D), garnet and the Mix, (Figs. 6C), plagioclase and the Mix (Fig. 7A). Fig. 6G corresponds to a representative portion of the Mix characterized by a relatively large proportion of glass and the segregation of melt pools ≈10-20 μm across, while Fig. 6H corresponds to a portion of the Mix far from the contact Mix–biotite, with a very low glass percentage. The SEM study shows also that: (i) melt films in between minerals can be as thin as a few (≤5) microns across (Figs. 6C, E, F), which are extremely difficult to detect via μ-XRF mapping; (ii) glass can be also mostly absent from some of the mineral boundaries (Fig. 7B); and (iii) the geometry of the glass network down to the micrometer scale is quite complex and irregular compared to equilibrium microstructures described in experiments (compare Figs. 6-7 with e.g. Fig. 5 from Laporte et al. 1997), even if experiments lasted days whereas, in the case of enclaves, geochronology suggests that melt coexisted with minerals at high temperature for a few million years.

4.2 Modal analysis

It is important to know the modal amount of phases in the enclave HO1, particularly the

glass percentage, in order to understand the controls on the distribution of melt recorded in these migmatites, and its role on the segregation of melt and on crustal rheology. Thus phase abundances were determined by both mass balance calculation and image analysis.

The mass balance calculation was performed by the spreadsheet MINSQ (Hermann and Berry 2002) which is a modification of the least squares method to quantitatively estimate the proportions of constituent minerals in rocks from bulk rock XRF chemical analysis and EMP mineral compositions. Table 1 reports the bulk composition of enclave HO1 from Ferri et al. (2007), and Table 2 shows representative compositions of the matrix glass and minerals used for the mass balance calculation. The selected composition for the matrix glass (Gl-3 in Table 2) was measured in HO1 next to a Grt and is similar to the average composition of matrix glass for this particular enclave, while the compositions of the minerals are from Cesare (2000) (enclave HO-42, Table 1 in Cesare 2000) who observed that the mineral chemistry of different Grt-Bt-Sil enclaves is very homogeneous. The calculated glass proportion is 8.9 wt.% (Table 3) together with 16.5 wt.% plagioclase, 22.4 wt.% biotite, 15.7 wt.% garnet, 24.9 wt.% sillimanite, 10.1 wt.% K-feldspar and 2.1 % of spinel. The content of ilmenite is virtually zero even if it is observed in limited amounts within the enclave. The residuals sum of squares (SSQ) of the mass balance calculation corresponds to 0.2.

The image analysis was performed using the ROIs definition and software ENVI® (see section 4.1) for the phases glass, biotite, garnet, sillimanite, plagioclase, K-feldspar, spinel and ilmenite. The results are reported in Table 3 for all thin sections. The area appearing as glass (e.g., the dark-red areas of Figs. 4D and 5C) is between 22-32 area % but does not necessarily correspond to pure glass, because glass may appear sometimes intermixed with minerals such as plagioclase (Figs. 6A, B) or sillimanite as in the Mix (Figs. 6C, D, F-G). Pools of pure glass, from tens up to a few hundred μm in diameter, are also observed. In order to get a more precise estimate of the proportion of glass, we constrained the amount of glass

in the Mix, and along the contacts between the biotite–plagioclase, biotite–garnet, and garnet–plagioclase pairs, as follows:

1) The glass content of the Mix was determined on selected areas of BSE images (e.g., Figs. 6D, E, G) with the software ImageJ® to be around 29 - 45 area %. This value is in excellent agreement with the 25-50 vol.% of glass in the Mix reported by Cesare et al. (1997), who expressed the chemical composition of the Mix from different areas as a linear combination of the compositions of matrix glass and sillimanite.

2) The glass proportion in pools and films between selected pairs of minerals, such as garnet – plagioclase (e.g., Fig. 6A) and biotite – plagioclase (e.g., Fig. 6B), varies between 40-100 area %.

Based on the previous considerations, the bulk content of glass in the rock was calculated as the sum of two contributions: (1) the glass within the Mix corresponding to an average of 40 area % of the Mix (red area of Fig. 5B), and (2) the glass along the mineral boundaries corresponding to an average of 70 area % (black area of Fig. 5B). The resulting glass percentage varies between 12.9 area % and 14.8 area % (Table 3). The glass content of the enclave HO1 calculated in this study is in agreement with the estimated glass proportion of 10-15% obtained from Rietveld refinement by Ferri et al. (2007), and with the 11 wt.% glass percentage calculated by mass balance for another Grt-Bt-Sil enclave from El Hoyazo (HO-50; Table 1 in Acosta-Vigil et al. 2010). Simple calculations considering the amount of sillimanite and mean proportion of glass in the Mix, indicate that most of the glass in the enclave (close to 10%) is present within the Mix, whereas glass as melt films and pools amounts up to a few %.

4.3 Microprobe analysis

An important topic regarding crustal anatexis is the composition of the primary melt and its variability throughout the anatectic area, controlled by the composition of the protolith, the

467 microstructural environment and the kinetics of melting (e.g. Acosta-Vigil et al. 2017). The
468 existence of melt compositional heterogeneities in major elements during anatexis at the grain
469 scale has been documented by Braun and Kriegsman (2001) via analyses of glass (quenched
470 melt) in anatectic metapelitic xenoliths brought to the surface by basanites. Other authors
471 have reported the preservation of major and trace element as well as isotopic heterogeneities
472 in apparently homogeneous granitic bodies; these heterogeneities have been interpreted as
473 inherited from their source area (e.g., Deniel et al. 1987; Pressley and Brown 1999; Clemens
474 and Benn 2010; Farina et al. 2014). Even though the compositional variations of the glass in
475 the studied enclave HO1 is beyond the main topic of this work, we have conducted glass
476 analyses at different microstructural locations of the interconnected glass network in the
477 enclave, located up to several mm apart from each other, and compared them to matrix glass
478 compositions in other Grt-Bt-Sil enclaves from El Hoyazo.
479 We analyzed the compositions of glasses at the contact with garnet, biotite, plagioclase and
480 the Mix. Fig. 7A reports the locations of glass analyses close to Pl and Sil, or in between the
481 two phases in section HO1XZ, and Fig. 7B shows the locations of glass analyses close to Grt
482 and Bt. Analyses show a relatively homogeneous major element composition of the glass,
483 independently of the nature of the adjacent mineral, with high SiO_2 (70-75 wt.%), Al_2O_3
484 (12.4-14.7 wt.%), K_2O (5.0-5.4 wt.%), P_2O_5 (0.5-0.6 wt.%) and #K (0.52-0.60), moderate to
485 low FeO_t (1.8-2.0 wt.%), and low MgO (0.15-0.19), CaO (0.3-0.5 wt.%) and #Mg (0.11-
486 0.16). The Aluminum Saturation Index (ASI) ranges between 1.10-1.30 and H_2O, calculated
487 by difference, between 1-6 wt.% (Table 4). It is interesting that matrix glass compositions in
488 this (HO1) and two other Grt-Bt-Sil enclaves (HO-50 and PFHz3) are quite similar, even if
489 these three enclaves represent decimetric fragments of a similar metasedimentary protolith
490 undergoing anatexis at the base of the continental crust, that were likely originally separated
491 in the source area at least some meters if not more (Fig. 8 and Table 5 Supplementary

492 Material).

493 **5. Discussion**

494 **5.1. Geometry of the microscopic-scale melt network and its origin**

495 On the basis of the μ-XRF mapping of major and trace element concentrations and SEM
496 observations, we were able to provide a reasonably detailed picture of the distribution of glass
497 (former melt) at the grain boundary scale within a migmatite represented by a Grt-Bt-Sil
498 anatectic enclave present within El Hoyazo dacites (SE Spain). Detailed petrologic and
499 geochemical studies have shown that during anatexis these rocks lost several tens of wt.% of
500 melt, implying that melt formed an interconnected network throughout the original protolith
501 at a scale larger than domains represented by the Grt-Bt-Sil enclaves (of cm-dm scale), and
502 that there was a driving force for melt segregation and extraction from these domains into
503 either other melt-enriched domains within the migmatite and/or out of the migmatite and into
504 the overlying subsolidus crust.

505 The estimated volume of glass in the enclave is ≈10-15 wt.%, well below that required for
506 isolation of individual grains within the melt and rock disaggregation (≈25%; e.g. Rosenberg
507 and Handy 2005), but similar or quite close to the minimum energy porosity for equilibrium
508 dihedral angles of ≈20-40° (≈12-22%; e.g. Laporte and Watson 1995). With this proportion of
509 melt and under textural equilibrium, melt should have formed during anatexis an
510 interconnected network of three-grain junctions channels and, in two dimensional sections of
511 the anatectic rocks, melt should mostly appear in three-grain junctions with cuspate
512 terminations and melt-solid-solid dihedral angles of 20-60° (Jurewicz and Watson 1984,
513 1985; Laporte and Watson 1995; Laporte et al. 1997; Holness 2006; Holness and Sawyer
514 2008; Holness et al. 2011).

515 This and previous studies (e.g. Cesare et al. 1997; Cesare and Gómez-Pugnaire 2001;

Cesare 2008) show however that glass forms thin coats around many of the minerals (e.g. Grt, Bt) and localizes along most of the grain boundaries, as a few to tens of μm–thick films, intermixtures and irregular or rounded tens to hundreds of μm-diameter pockets. In detail and down to the micrometer scale, the geometry of the melt network is quite complex and irregular (Figs. 6 and 7) even if a tendency to develop low apparent dihedral angles can be observed (Figs. 6E, F, 7B). In addition sillimanite and the glass form a fine-grained felt (the "Mix"), with glass proportion increasing towards the mineral grains (e.g. biotite) rims (Figs. 6C, D, F, G) and segregation of some local glass pockets (Fig. 6E, F). Nearly pure sillimanite (i.e. mostly glass-free Mix) is observed away from Mix-mineral boundaries (Fig. 6H), corresponding to the grey areas of Figs. 4D and 5C. Glass films and pockets seem to form a pervasive and mostly interconnected network in between the major minerals throughout the studied sample, due mostly to the crosscutting of melt films and pools parallel and at high angle with the main foliation, with some glass-rich domains reaching dimension of up to a few hundred micrometers (Fig. 6). Previous studies have also described glass-filled discontinuities, ≤50 μm-thick and a few mm-long, oriented at high angle with respect to the main foliation, that likely connected melt films parallel to foliation during anatexis (Fig. 4f of Cesare et al. 1997).

These observations indicate that the grain-scale distribution of melt in the studied migmatite is not in textural equilibrium with the solid residue. Given that enclaves show in general quite homogeneous mineral compositions recording peak or close to peak P-T conditions, and that former melt solidified to glass with very minor crystallization (Cesare et al. 1997; Cesare 2008; Acosta-Vigil et al. 2007, 2010), this implies that: (i) enclaves were quenched during extrusion while having the mineral assemblage and mineral compositions of, or close to, peak P-T conditions; (ii) the timeframes between entrainment in the dacitic magma and extrusion were short (≤10^3-10^4 years for the particular case of Grt-Bt-Sil enclaves

showing post-deformation coronitic microstructures around Grt or reaction rims between Bt-Sil, interpreted to have occurred after entrainment within the host dacite: Cesare 2008; Alvarez-Valero et al. 2005, 2007; these static microstructures are absent in the studied enclave, and hence its ascent and extrusion could be even faster); (iii) although some modifications might have occurred after entrainment and during ascent, the reported grain-scale glass distribution should largely reflect the distribution of melt at or close to peak anatectic conditions during anatexis due to fluid-absent, breakdown-melting of biotite, as melt did not have time to react back with the residue or crystallize, as it happens during slow cooling of anatectic terranes; and (iv) hence the melt network did not achieve microstructural equilibrium with the residue during regional anatexis of these rocks, even if geochronological studies have inferred that melt resided within its source area in contact with the solid residue for about 3 Ma (Cesare et al. 2003b).

The observation that the melt network seems still largely interconnected indicates that this network did not collapse, likely implying that melt was being produced within, and flowing throughout the protolith in the lower continental crust right before disaggregation and entrainment of fragments into the magma. Once into the magma, hydrostatic stress prevented any further intergranular melt flow or, at least, melt segregation out of the residual enclave. These observations, together with the homogeneity of matrix glass throughout the enclave, and similarity with matrix glass compositions from other Grt-Bt-Sill enclaves, suggest that the composition of the matrix glass is close to that of the primary melt being produced during anatexis of the protolith right before entrainment into the magma (see Sawyer 2001), and that it might not strictly represent melt produced in situ but within adjacent domains, as an example of a quenched inter-granular melt flow through a residual migmatite in its way towards e.g. macroscopic leucosomes. In this context, matrix melt homogeneity might not only be due to small minimum volumes for equilibration and associated short diffusion

distances (Acosta-Vigil et al. 2017) but also to mechanical mixing during inter-granular flow.

The above observations indicate that melt can form an interconnected network even if melt-residue textural equilibrium has not been achieved. Previous experimental programs dealing with the disequilibrium partial melting of macroscopic solid cylinders of crustal protoliths under hydrostatic conditions have already described the development of an interconnected melt network at low degrees of partial melting (Wolf and Wyllie 1991; Acosta-Vigil et al. 2006). This in turn has implications for the rapid segregation and extraction of melt from migmatites before any major melt-residue equilibration has taken place and, together with slow diffusion in crystals and lack of major recrystallization of the residue (e.g. Acosta-Vigil et al. 2017), may explain the fact that chemical disequilibrium between melt and residue seems to be the rule rather than the exception (Bea 1996).

Previous studies of melt pseudomorphs in migmatites and granulites (Sawyer 2001; Marchildon and Brown 2002; Holness and Sawyer 2008) show the following similarities with the El Hoyazo enclaves regarding inferred former melt distributions: (i) in most cases melt pseudomorphs seem to record melt-solid residue disequilibrium textural distributions, with melt films located along many grain boundaries, due mostly to lack of achievement of textural equilibrium during anatexis; (ii) the distribution of melt is in most cases controlled by the rock fabric developed during syn-anatectic deformation, with melt films preferentially located along grain boundaries parallel to that fabric (foliation, shear surfaces), which are thinner and longer with respect to those perpendicular to it. There are, however, some differences, including: (i) the melt proportion found in the residual enclaves (10-15 %) is similar or higher with respect to described melt proportions in residual domains of studied migmatites (2-12 %); (ii) this ≈10-15% of melt left in the residual enclaves forms mostly an interconnected network, whereas similar to lower proportions of melt in residual migmatites (2-12 %) form small ≈0.1-1 mm across interconnected branching networks, separated by basically melt-

absent regions ≈0.5-2 mm in size. This difference might be due in part to the entrainment of enclaves within the dacite magma before the collapse of the grain-scale melt drainage network. Overall though, the studies of both melt pseudomorphs in migmatites and granulites of anatectic terranes, and grain-scale glass distribution in the residual anatectic enclaves of El Hoyazo, seem to indicate that textural melt-residue equilibrium during crustal anatexis might not be as common as we initially thought. Coupled with experimental studies on rock core melting indicating interconnection at low degrees of melting of a melt network in textural disequilibrium with the residue (Wolf and Wyllie 1991; Acosta-Vigil et al. 2006), it indicates that melt-residue textural disequilibrium during anatexis does not prevent from rapid melt interconnection and segregation. Indeed more studies of melt pseudomorphs in migmatites are required to asses the extent of textural equilibration during crustal anatexis and its role of melt segregation/extraction, melt compositions, and crustal rheology (Sawyer 2001, 2014; Marchildon and Brown 2002; Holness and Sawyer 2008).

Regarding the architecture and microscale-to-mesoscale connection of the melt drainage network in anatectic terranes, it is worth pointing out that the grain-scale glass network mapped in the enclave via μ-XRF resembles the mesoscale interconnected network of deformation bands (leucosomes) in migmatites (Brown 2007); thus glass is dominantly located in films and domains parallel to foliation (compaction bands), which are connected by films and pools oblique to foliation. This might suggest that grain-boundary melt flow parallel to the main fabric might be as important as perpendicular flow to segregate and drain melt out of migmatite residual domains. The flow perpendicular to the main fabric perhaps dominates at ≤5 mm away from the contact with leucosomes (Sawyer 2001) while branching of the melt network may become important mostly after melt leaves the suprasolidus crust.

5.2. Anatexis, deformation and melt drainage

The El Hoyazo enclaves provide the opportunity to constraint the melt drainage history

616 during the anatexis of this particular rock, by integrating the analysis of the distribution of
617 glass and the multistage melting history reported by the abundant previous literature dealing
618 with the microstructures, petrology, geochemistry and geochronology of these quenched
619 migmatites (e.g. Cesare et al. 1997, 2003b, 2005; Cesare and Maineri 1999; Cesare and
620 Gómez-Pugnaire 2001; Zeck and Williams 2002; Álvarez-Valero et al. 2005, 2007; Acosta-
621 Vigil et al. 2007, 2010, 2012; Cesare 2008; Tajcmanová et al. 2009; Álvarez-Valero and
622 Waters 2010; Ferrero et al. 2011; Bartoli 2017).
623 Cesare et al. (1997) and Cesare and Gómez -Pugnaire (2001) demonstrated that partial
624 melting took place mostly under stress and associated deformation of the protolith
625 (syntectonic melting), on the base of several microstructural features:
626 a) The presence of a well-developed main foliation, generally marked by subparallel
627 crystals of biotite, graphite and acicular sillimanite, in which the biotite flakes contain MI and
628 are commonly deflected;
629 b) The biotite foliation anastomoses around garnet porphyroblasts which contain MI as
630 well, or around knots of acicular sillimanite immersed in interstitial melt which presumably
631 pseudomorphs pre-existing garnets (see reaction (5) in Acosta-Vigil et al., 2010);
632 c) The matrix glass occurs along thin foliation-parallel layers and in strain shadows around
633 garnet. Relicts of an earlier foliation can be observed in the strain shadows around garnet and
634 within microlithons in the main foliation. The earlier foliation is marked by graphite and
635 biotite, which is involved in iscoclinal folding and slight crenulation. Minerals of the earlier
636 foliation also contain MI or are intergrown with glass, but are generally undeformed;
637 d) In some cases, glass occurs in apparently extensional discontinuities at high angle with
638 the foliation, sometimes appearing as result of boudinage.
639 All these observations imply that MI and at least part of the matrix glasses were generated
640 in a regional metamorphic setting previously to or during the deformation that produced the

main foliation in the anatectic metapelites (Cesare et al. 1997, 2003b; Cesare and Maineri 1999; Cesare 2000; Cesare and Gómez-Pugnaire 2001; Acosta-Vigil et al. 2007; Acosta-Vigil et al. 2010). Since the foliation postdates or is synchronous with anatexis, it follows that the enclaves deformed and partially melted before being enclosed in the host dacite (Cesare and Gómez-Pugnaire 2001).

The sequence of melt producing reactions taking place during the prograde history of the Grt-Bt-Sil enclaves was reconstructed on the base of the major and trace element compositions of MI preserved in plagioclase and garnet, and intergranular glass films. It was concluded that MI in plagioclase reflect the earliest granitic melts produced at ≈700 °C by fluid-present melting of muscovite evolving rapidly to fluid-absent conditions, whereas MI in garnet were produced concomitantly or slightly later via fluid-absent breakdown-melting of muscovite at ≈750°C. The intergranular melt represents the latest melt produced by fluid-absent breakdown-melting of biotite starting at ≈800 °C and ending at peak conditions of ≈850 ± 50 °C and 0.5-0.7 GPa (Cesare et al. 1997, 2005; Acosta-Vigil et al. 2007, 2010; Ferrero et al. 2011). Cesare and Maineri (1999) suggested that the temperature overstepping for the enclaves was very high, so it is very likely that most of the prograde melting reactions actually occurred simultaneously. A minority of enclaves record a final static decompression event, likely occurring after incorporation in the host dacite magma, at ≈820 °C and < 0.5 GPa, as evidenced by the presence of Spl + Ilm + Crd + feldspar + melt coronas after Grt (Alvarez-Valero et al. 2007).

Acosta- Vigil et al. (2010) reconstructed the melt production during prograde heating and determined that ~20 wt.% of anatectic melt was produced by muscovite fluid-present melting, ~25 wt.% by muscovite fluid-absent melting and ~15 wt.% by biotite fluid-absent melting, making about 60 wt.% of total melt. Such percentage is in good agreement with the estimate of Cesare et al. (1997) who suggested that the enclaves experienced about 40 – 60% melt

666 extraction that was assisted by deformation. The volume of melt produced after the enclaves
667 were incorporated into the dacitic magma was not constrained by Cesare et al. (1997) or
668 Acosta-Vigil et al. (2010), but it may reasonably be limited to a few percentages (< 3 - 4
669 wt.%) based on: 1) microstructural observations and algebraic calculations based on reaction
670 coronas around Grt (Alvarez-Valero et al. 2007); and 2) thermodynamic modelling and
671 isopleths calculated by Bartoli (2017). No retrogressive coronas after Grt were observed,
672 however, in the analyzed thin sections of sample HO1.

673 The amount of glass retained within the sample HO1, constrained by combination of μ-
674 XRF chemical maps, image analysis, mass balance calculation and XRPD Rietveld
675 refinement (Ferri et al. 2007) is ≈10-15 wt.%. If we combine this value with previous
676 estimations of melt produced and extracted from these residual rocks, and exclude the small
677 percentage of melt potentially formed during static melting during transport to the surface, we
678 infer that a considerable proportion of the melt produced during regional metamorphism was
679 not extracted from the protolith represented by the Grt-Bt-Sil enclaves but stored at deep
680 crustal levels, when the crust was still deforming at the regional scale. These melt percentages
681 are high compared to the proportion of melt required for melt interconnection in anatectic
682 crustal protoliths (<1 to a few volume %; e.g. Wolf and Wyllie 1991; Laporte et al. 1997;
683 Acosta-Vigil et al. 2006), and have been described as well in some residual though contact
684 anatectic migmatite (≈12 %; Sawyer 2001).

685 The above observation seems to contradict the generally accepted idea that, once melt
686 becomes interconnected, and in the presence of a differential stress, the proportion of melt
687 above the permeability threshold can be rapidly segregated from the solid residue (e.g.
688 Clemens and Stevens 2016). Laporte et al. (1997) argued that melt segregation might be
689 inefficient at such low degrees of melting due to the high viscosity of granite melt, and that
690 there might be a range of melt percentages above the percolation threshold (≈5-10 vol.%)

691 over which melt is interconnected but nearly stagnant. They suggested that it would be melt
692 viscosity, instead of melt interconnection, that should be the limiting factor in the segregation
693 of granitic melts from its source area. This could be applied to the case of the El Hoyazo
694 enclaves, though there might be at least two other reasons for the high proportion of melt
695 present in these regionally metamorphosed residual migmatites: the timing of melting versus
696 fragmentation and incorporation into the dacite magma; and the presence of particular
697 microstructures in the rock that favoured melt retention. This is explained below.
698 The protolith represented by the Grt-Bt-Sil enclaves may have been disaggregated and
699 included into the dacitic magma while melt was being produced within, and flowing through
700 the residual anatectic rock, before any major collapse of the melt network, as suggested by the
701 observed interconnection of the grain-scale glass network (see above).
702 The enclaves have abundant fine-grained sillimanite needles intermixed with glass in
703 variable proportions (the Mix), which may have resulted from muscovite-breakdown melting
704 reaction involving Ms + Pl + Qtz (compare with microstructures in Patiño Douce and Harris
705 1998; Buick et al. 2004), and hence formed at the onset of anatexis (see Acosta-Vigil et al.
706 2010). Based on conclusions on melt production from Acosta-Vigil et al. (2010) (see above)
707 and observations from the present manuscript, a large proportion of melt formed during these
708 muscovite melting reactions should have been segregated from the protolith. The Mix,
709 however, might have played a significant role regarding the accumulation and retention of
710 some of this melt. Because of the high aspect ratio and apparently random orientation of
711 sillimanite needles in the Mix (Figs. 6C, D, G, H; see also Fig. 3b of Cesare et al. 1997), this
712 mineral frame can accommodate variable porosities and store elevated proportions of melt
713 when such porosity is high. In fact, a large proportion of the glass present in the enclaves
714 seems to be located within the Mix (see above). The rheology of the Mix during syn-anatectic
715 deformation might have been different from that of the biotite+melt domains, and the enclave

716 may have behaved as a composite material with an inhomogeneous distribution of matrix
717 stiffness. Bons and Urai (1994) reported rock analogue deformation experiments on a two-
718 phase system represented by mixtures of camphor and octachloropropane (OCP) in different
719 proportion, as representative of rocks close to their melting temperature. Despite the higher
720 rheological complexity of the El Hoyazo enclave containing also garnet and plagioclase as
721 major minerals, the comparison between Fig. 5C and Fig. 2 of Bons and Urai (1994) suggests
722 that during anatexis the enclaves were likely constituted by two principal domains in terms of
723 matrix stiffness, the Mix (+ Grt + Pl?) with higher stiffness and the biotite (+ melt) with lower
724 stiffness. Thus it is possible that the presence of the Mix from the initial stages of anatexis
725 prevented a proportion of the melt from being easily segregated, in a similar fashion as
726 Sawyer (2014) described how another microstructure –an infertile framework made of
727 plagioclase+cordierite, constituting ≈40-60% of the rock and representing impermeable and
728 strong rock domain enclosing smaller volumes of fertile material– delayed compaction-driven
729 melt segregation in contact metamorphic migmatites developed at the base of the Duluth
730 Complex, Minnesota.

731 **6. Implications and conclusions**

732 This study likely provides the closest picture we have so far for the syn-anatectic grain-
733 scale distribution of melt during regional metamorphism at or close to peak conditions, by
734 mapping the distribution of glass in quenched migmatites from El Hoyazo using synchrotron
735 μ-XRF. The study has implications for three main topics: (i) the architecture of the melt
736 drainage network during anatexis of the continental crust, (ii) the extent of melt-residue
737 textural equilibration during crustal anatexis, and (iii) the composition of the melt and extent
738 of melt-residue chemical equilibration during anatexis before melt segregates from its source.

739 This study indicates that the distribution of melt is largely controlled by syn-anatectic
740 deformation and orientation of the associated foliation and potential dilation/shear surfaces at

high angle to the foliation. Interconnection of the grain-scale melt network is due to the crosscutting of melt films and pools located along these deformation-related microstructures: foliation and dilation/shear surfaces. This pattern resembles the mesoscale interconnected network of leucosomes described in migmatites, and suggests that grain-boundary melt flow parallel to the main fabric (e.g. foliation) might be as important as flow perpendicular to it in order to drain melt out of migmatite residual domains. It follows that branching of the melt network may become important mostly after the melt leaves the suprasolidus crust. This dominant pattern for the grain-scale distribution of the melt is somewhat modified by: metamorphic microstructures such as the presence of porphyroblast or mineral aggregates (e.g. the Mix, an intimate intergrowth between melt and fibrolitic sillimanite), that truncate foliation or along which foliation anastomoses; and the nature of the Mix, which may become important to store melt in migmatites during syn-anatectic deformation above the small percentages required for melt interconnection.

Contrary to the apparently general consensus (e.g. Laporte and Watson 1995; Laporte et al. 1997), and in accordance with most of the findings during studies of melt pseudomorphs in migmatites of anatectic terranes (Sawyer 2001; Marchildon and Brown 2002; Holness and Sawyer 2008), melt and mineral residue did not reach textural equilibration during anatexis of the El Hoyazo enclaves. However, melt was extracted from most of these migmatites as their residual nature indicates, implying melt interconnection at some point. Melt-residue textural equilibrium guarantees melt interconnection at low degrees of partial melting (e.g. Laporte and Watson 1995; Laporte et al. 1997; Holness et al. 2011). Experimental studies on the melting of solid rock cores, however, indicate that melt interconnection can be reached at low degrees of melting as well even if melt-residue textural equilibrium has not been achieved, in the case of both lineated amphibolites (Wolf and Wyllie 1991) and isotropic granites (Acosta-Vigil et al. 2006). This observation might be important for the rapid segregation and

766 extraction of melt from the source rock during crustal anatexis, and explain the current
767 general consensus that melt-residue chemical disequilibrium during anatexis is the rule rather
768 than the exception (Bea 1996).

769 Previous studies of melt pseudomorphs in migmatites of anatectic terranes have found the
770 same picture regarding the controls of deformation, foliation and metamorphic
771 microstructures on the grain-scale distribution of melt, and regarding the extent of mineral-
772 melt textural equilibration during anatexis (Sawyer 2001, 2014; Marchildon and Brown 2002;
773 Holness and Sawyer 2008). Indeed more of these detailed studies of melt pseudomorphis in
774 migmatites are needed to assess issues such as whether textural disequilibrium during
775 anatexis is the rule rather that the exception, and the role of grain-scale melt distribution on
776 melt composition, extent of melt-residue equilibration before melt segregation, and crustal
777 rheology (Sawyer 2001; Marchildon and Brown 2002).
778

779 **AKNOWLEDGMENTS**

780 This work was funded by the Proyecto FAPA, Universidad de Los Andes (Bogotá,
781 Colombia); the Centro Nacional de Pesquisa em Energia e Materiais, Brazilian Synchrotron
782 Light Laboratory (LNLS), proposal n. XAFS1 – 17105; the CARIPARO (Cassa di Risparmio
783 di Padova e Rovigo) project MAKEARTH. We are grateful to Charles LeLosq for advice on
784 granite glass properties, two anonymous reviewers that provided numerous comments and
785 suggestions on a previous version of this manuscript, Bernardo Cesare, an anonymous
786 reviewer for their thorough and positive reviews; all of them greatly improved the original
787 manuscript. S. Penniston-Dorland is thanked for insightful review and very careful editorial
788 handling.

789 **REFERENCES**

790 Acosta-Vigil, A., Buick, I., Hermann, J., Cesare, B., Rubatto, D., London, D., and Morgan,

791 G.B. VI (2010) Mechanisms of crustal anatexis: a geochemical study of partially melted
792 metapelitic enclaves and host dacite, SE Spain. Journal of Petrology, 51, 785-821.
793
794 Acosta-Vigil, A., Buick, I., Cesare, B., London, D., and Morgan, G.B. (2012) The extent
795 of equilibration between melt and residuum during regional anatexis and its implications for
796 differentiation of the continental crust: A study of partially melted metapelitic enclaves.
797 Journal of Petrology, 53, 1319-1356.
798
799 Acosta-Vigil, A., Cesare, B., London, D., and Morgan, G.B. VI (2007) Microstructures
800 and composition of melt inclusions in a crustal anatectic environment, represented by
801 metapelitic enclaves within El Hoyazo dacites, SE Spain. Chemical Geology, 237, 450-465.
802
803 Acosta-Vigil, A., Cesare, B., London, D., and Morgan, G.B., VI, Cesare, B., Hermann, J.,
804 Bartoli, O. (2017) Primary crustal melt compositions: Insights into the controls, mechanisms
805 and timing of generation from kinetics experiments and melt inclusions. Lithos, 286-287,
806 454-479.
807
808 Acosta-Vigil, A., London, D., and Morgan, G.B., VI (2006) Experiments on the kinetics of
809 partial melting of a leucogranite at 200 MPa H_2O and 690-800°C: Compositional variability
810 of melts during the onset of H_2O-saturated crustal anatexis. Contribution to Mineralogy and
811 Petrology, 151, 539-557
812
813 Álvarez-Valero, A. M. and Kriegsman, L. M. (2007) Crustal thinning and mafic
814 underplating beneath the Neogene Volcanic Province (Betic Cordillera, SE Spain): Evidence
815 from crustal xenoliths. Terra Nova, 19, 266-271.

Álvarez-Valero, A. M. and Kriegsman, L. M. (2008) Partial crustal melting beneath the Betic Cordillera (SE Spain): The case study of Mar Menor volcanic suite. Lithos 101, 379-396.

Álvarez-Valero, A.M. and Waters, D.J. (2010) Partially melted crustal xenoliths as a window into sub-volcanic processes: Evidence from the Neogene Magmatic Province of the Betic Cordillera, SE Spain. Journal of Petrology, 51, 973-991.

Álvarez-Valero, A. M., Cesare, B., and Kriegsman, L.M. (2005) Formation of elliptical garnet in a metapelitic enclave by melt-assisted dissolution and reprecipitation. Journal of Metamorphic Geology, 23, 65-74.

Álvarez-Valero, A. M., Cesare, B. and Kriegsman, L. M. (2007) Formation of spinel-cordierite-feldspar-glass coronas after garnet in metapelitic xenoliths: reaction modeling and geodynamic implications. Journal of Metamorphic Geology, 25, 305-320.

Barbey, P., Bertrand, J.-M., Angoua, S. and Dautel, D. (1989) Petrology and U/Pb geochronology of the Telohat migmatites, Aleksod, Central Hoggar, Algeria. Contributions to Mineralogy and Petrology, 101, 207–219.

Bartoli, O. (2017) Phase equilibria modeling of residual migmatites and granulites: an evaluation of the melt-reintegration approach. Journal of Metamorphic Geology, 35, 919-942.

Bea, F. (1996) Controls on the trace element composition of crustal melts. Transactions of

the Royal Society of Edinburgh: Earth Sciences, 87, 33–41.

Bons, P.D., and Urai, J.L. (1994) Experimental deformation of two-phase rock analogues. Materials Science and Engineering, A175, 221-229.

Braun, I. and Krlegsman, L.M. (2001) Partial Melting in Crustal Xenoliths and Anatectic Migmatites: A Comparison. Physics and Chemistry of the Earth (A), 26, 261-266.

Brown, M. (1994) The generation, segregation, ascent and emplacement of granite magma: the migmatite-to-crustally-derived granite connection in thickened orogens. Earth-Science Reviews, 36 (1-2), 83-130

Brown, M. (2004) The mechanism of melt extraction from lower continental crust of orogens. Transactions of the Royal Society of Edinburgh: Earth Sciences, 95, 35-48.

Brown, M., and Solar, G.S. (1998) Shear zone systems and melts: feedback relations and self-organization in oregenic belts. Journal of Structural Geology 20, 211–227.

Brown, M., and Solar, G.S. (1999) The mechanism of ascent and emplacement of granite magma during transpression: a syntectonic granite paradigm. Tectonophysics, 312, 1–33.

Brown,.M., Averkin, Y.A., McLellan, E.L., Sawyer, E.W. (1995) Melt segrergation in migmatites. Journal of Geophysical Research 100(B8), 15655-15679.

Brown, M.A., Brown, M., Carlson, W.D., and Denison, C. (1999) Topology of syntectonic melt-flow networks in the deep crust: Inferences from three-dimensional images of leucosome

867 geometry in migmatites. American Mineralogist, 84, 1793–1818.
868
869 Brown, M., Korhonen, F.J., and Siddoway, C.S. (2011) Organizing melt flow through the
870 crust. Elements 7, 261-266.
871
872 Brown, C.R., Yakymchuk, C., Brown, M., Fanning, C.M., Korhonen, F.J., Piccoli, P.M.,
873 and Siddoway, C.S. (2016). From source to sink: petrogenesis of Cretaceous anatectic
874 granites from the Fosdick migmatite-granite complex, West Antarctica. Journal of Petrology,
875 57, 1241–1278.
876
877 Buick, I. S., Stevens, G., and Gibson, R. L. (2004) The role of water retention in the
878 anatexis of metapelites in the Bushveld Complex Aureole, South Africa: an experimental
879 study. Journal of Petrology, 45, 1777-1797.
880
881 Carvalho, B.B., Sawyer, E.W., and Janasi, V.A. (2016) Crustal reworking in a shear zone:
882 transformation of metagranite to migmatite. Journal of Metamophic Geology,
883 http://dx.doi.org/10.1111/jmg.12180.
884
885 Cesare, B. (2000) Incongruent melting of biotite to spinel in a quartz-free restite at El
886 Joyazo (SE Spain): textures and reaction characterization. Contributions to Mineralogy and
887 Petrology, 139, 273–284.
888
889 Cesare, B. (2008) Crustal melting: working with enclaves. In: E.W. Sawyer and M. Brown,
890 Eds., Working with Migmatites. Mineralogical Association of Canada, Short Course Series,
891 38, 37–55.
892

Cesare, B. and Acosta-Vigil A. (2011) Using melt inclusions for understanding crustal melting processes. McGraw-Hill Yearbook of Science and Technology, 355-359.

Cesare, B. and Gómez-Pugnaire, M. T. (2001) Crustal melting in the Alborán domain: constraints from enclaves of the Neogene Volcanic Province. Physics and Chemistry of the Earth, 26, 255–260.

Cesare, B. and Maineri, C. (1999) Fluid-present anatexis of metapelites at El Joyazo (SE Spain): constraints from Raman spectroscopy of graphite. Contributions to Mineralogy and Petrology, 135, 41–52.

Cesare, B., Cruciani, G., and Russo, U. (2003a) Hydrogen deficiency in Ti- rich biotite from anatectic metapelites (El Joyazo—SE Spain): crystal-chemical aspects and implications for high-temperature petrogenesis. American Mineralogist, 88, 583–595.

Cesare, B., Gómez-Pugnaire, M.T., and Rubatto, D. (2003b) Residence time of S-type anatectic magmas beneath the Neogene Volcanic Prov- ince of SE Spain: a zircon and monazite SHRIMP study. Contributions to Mineralogy and Petrology, 146, 28–43, doi:10.1007/s00410-003-0490-x.

Cesare, B., Meli, S., Nodari, L., and Russo, U. (2005) Fe3+ reduction during biotite melting in graphitic metapelites: another origin of CO_2 in granulites. Contributions to Mineralogy and Petrology, 149, 129–140.

Cesare B., Rubatto D., and Gómez-Pugnaire M.T. (2009) Do extrusion ages reflect magma generation processes at depth? An example from SE Spain. Contributions to Mineralogy and Petrology, 157, 267-279.

Cesare, B., Salvioli Mariani, E., and Venturelli, G. (1997) Crustal anatexis and melt extraction during deformation in the restitic xenoliths at El Joyazo (SE Spain). Mineralogical Magazine, 61, 15–27.

Chappell, B.W., White, A.J.R., and Wyborn, D. (1987). The importance of residual source material (restite) in granite petrogenesis. Journal of Petrology, 28, 1111–1138.

Clemens, J.D., and Benn, K. (2010) Anatomy, emplacement and evolution of a shallow-level, post-tectonic laccolith: the Mt Disappointment pluton, SE Australia. Journal of the Geological Society, London, 167, 915–941.

Clemens, J. D., and Holness, M.B. (2000) Textural evolution and partial melting of arkose in a contact aureole: a case study and implications. Electronic Geosciences, 5, 4.

Clemens, J.D. and Stevens, G. (2016) Melt segregation and magma interactions during crustal melting: Breaking out the matrix. Earth-Science Reviews, 160, 333-349.

Collins, W.J., and Sawyer, E.W. (1996) Pervasive magma transfer through the lower–middle crust during non-coaxial compressional deformation: an alternative to diking. Journal of Metamorphic Geology, 14, 565–579.

943 Deniel, C., Vidal, P., Fernandez, A., Lefort, P. and Pecaut, J.J. (1987) Isotopic study of the
944 Manaslu granite (Himalaya, Nepal): inferences of the age and source of Himalayan
945 leucogranites. Contributions to Mineralogy and Petrology, 96, 78–92.

946

947 Farina, F., Dini, A., Rocchi, S., and Stevens, G. (2014) Extreme mineral-scale Sr isotopic
948 heterogeneity in granites by disequilibrium melting of the crust. Earth and Planetary Science
949 Letters, 399, 103-115.

950

951 Ferrero, S., Bodnar, R.J., Cesare, B., and Viti, C. (2011) Reequilibration of primary fluid
952 inclusions in peritectic garnet from metapelitic enclaves, El Hoyazo, Spain. Lithos, 124, 117–
953 131.

954

955 Ferri, F., Burlini, L., Cesare, B., and Sassi, R. (2007) Seismic properties of lower crustal
956 xenoliths from El Hoyazo (SE Spain): experimental evidence up to partial melting. Earth and
957 Planetary Science Letters, 253, 239–253.

958

959 Garcia-Arias, M., and Stevens, G. (2016) Phase equilibrium modelling of granite magma
960 petrogenesis: A. An evaluation of the magma compositions produced by crystal entrainment
961 in the source. Lithos, doi: 10.1016/j.lithos.2016.09.028.

962

963 Giordano, D., Russell, J.K., and Dingwell, D.B. (2008) Viscosity of magmatic liquid: a
964 model. Earth and Planetary Science Letters, 271, 123-134.

965

966 Guernina, S., and Sawyer, E.W (2003) Large-scale melt-depletion in granulite terranes: an
967 example from the Archean Ashuanipi Subprovince of Quebec. Journal of Metamorphic

968 Geology, 21, 181–201.
969
970 Harte, B., Hunter, R. H. and Kinny, P. D. (1993) Melt geometry, movement and
971 crystallisation, in relation to mantle dykes, veins and metasomatism. Philosophical
972 Transactions of the Royal Society of London, 342, 1-21.
973
974 Hermann, W., and Berry, R.F. (2002) MINSQ – a least squares spreadsheet method for
975 calculating mineral proportions from whole rock major element analyses. Geochemistry:
976 Exploration, Environment, Analysis, 2, 361–368.
977
978 Holness, M.B., (2006) Melt-solid dihedral angles of common minerals in natural rocks.
979 Journal of Petrology, 47, 791-800.
980
981 Holness, M.B., and Sawyer, E.W. (2008) On the pseudomorphing of melt-filled pores
982 during the crystallization of migmatites. Journal of Petrology, 49, 1343–1363.
983
984 Holness, M.B., Cesare, B., Sawyer, E.W. (2011) Melted rocks under the microscope:
985 Microstructures and their interpretation. Elements, 74, 247-252.
986
987 Jurewicz, S.R., and Watson, E.B. (1984) Distribution of partial melt in a felsic system: the
988 importance of surface energy. Contributions to Mineralogy and Petrology, 85, 25-29.
989
990 Jurewicz, S.R., and Watson, E.B. (1985) The distribution of partial melt in a granitic
991 system: the application of liquid phase sintering theory. Geochimica et Cosmochimica Acta,
992 49, 1109-1121.
993

Laporte, D., and Watson, E.B. (1995). Experimental and theoretical contraints on melt distribution in crustal sources: the effect of crystalline anisotropy on melt interconnectivity. Chemical Geology, 124, 161-184.

Laporte, D., Rapaille, C., and Provost, A. (1997) Wetting angles, equilibrium melt geometry, and the permeability threshold of partially molten crustal protoliths. In: Bouchez, J.L., Hutton, D.H.W., Stephens, W.E. (Eds.), Granite: From Segregation of Melt to Emplacement Fabrics, p. 31-54. Kluwer Academic Publishers, Dordrecht, The Netherlands.

Lopez Ruiz, J., and Rodriguez Badiola, E. (1980) La región volcánica Neógena del sureste de España. Estudios Geològicos, 36, 5–63.

Marchildon, N., and Brown, M. (2002) Grain-scale melt distribution in two contact aureole rocks: implication for controls on melt localization and deformation. Journal of Metamorphic Geology, 20, 381–396.

Marchildon, N., and Brown, M. (2003) Spatial distribution of melt-bearing structures in anatectic rocks from Southern Brittany: Implications for melt transfer at grain- to orogen-scale. Tectonophysics, 364, 215–235, doi:10.1016/S0040-1951(03)00061-1.

McLellan, E.L. (1988) Migmatite structures in the Central Gneiss Complex, Boca de Quadra, Alaska. Journal of Metamorphic Geology, 6, 517–542.

Morfin, S., Sawyer, E.W., and Bandyayera, D. (2014) The geochemical signature of a felsic injection complex in the continental crust: Opinaca Subprovince, Quebec. Lithos, 196–197, 339–355.

Morgan, G.B., VI and London, D. (1996) Optimizing the electron microprobe analysis of hydrous alkali aluminosilicate glasses. American Mineralogist, 81, 1176–1185.

Morgan, G.B., VI, and London, D. (2005) The effect of current density on the electron microprobe analysis of alkali aluminosilicate glasses. American Mineralogist, 90, 1131–1138.

Olivier, N.H.S. and Barr, T.D. (1997) The geometry and evolution of magma pathways through migmatites of the Halls Creek Orogen, Western Australia. Mineralogical Magazine, 61, 3-14.

Patiño Douce, A. E. and Harris, N. (1998) Experimental constraints on Himalayan anatexis. Journal of Petrology, 39, 689-710.

Perez, C.A., Radtke, M., Sanchez, H.J., Tolentino, H., Neuenshwander, R.T., Barg, W., Rubio, M., Bueno, M.I.S., Raimundo, I.M., and Rohwedder, J.J.R. (1999) Synchrotron radiation X-ray fluorescence at the LNLS: beamline instrumentation and experiments. X-Ray Spectrometry, 28, 320–326.

Pressley, R.A., and Brown, M. (1999) The Phillips pluton, Maine, USA: evidence of heterogeneous crustal sources and implications for granite ascent and emplacement mechanisms in convergent orogens. Lithos, 46, 335–366.

Rosenberg, C. L., and Handy, M.R. (2005) Experimental deformation of partially melted granite revisited: implications for the continental crust. Journal of Metamorphic Geology, 23,

19-28.

Rutter, E., and Neumann, D. (1995) Experimental deformation of partially molten Westerly granite under fluid-absent conditions, with implications for the extraction of granitic magmas. Journal of Geophysical Research, 100, 697–715.

Sawyer, E.W. (1991) Disequilibrium melting and the rate of melt-residuum separation during migmatization of mafic rocks from the Grenville Front, Quebec. Journal of Petrology, 32, 701–738.

Sawyer, E.W. (1994) Melt segregation in the continental crust. Geology, 22, 1019–1022.

Sawyer, E.W. (2001) Melt Segregation in the Continental Crust: Distribution and Movement of Melt in Anatectic rocks. Journal of Metamorphic Geology, 19, 291–309.

Sawyer, E.W. (2008) Working with migmatites: nomenclature for the constituent part. In: Sawyer, E. W., and Brown, M. (eds) Working with Migmatites. Mineralogical Association of Canada, Short Course Series 38.

Sawyer, E.W. (2014) The inception and growth of leucosomes: microstructure at the start of melt segregation in migmatites. Journal of Metamorphic Geology, 32, 695–712.

Solar, G.S., and Brown, M. (2001) Deformation partitioning during transpression in response to Early Devonian oblique convergence, northern Appalachian orogen, USA. Journal of Structural Geology, 23, 1043–1065.

Solé, V.A., Papillon, E., Cotte, M., Walter, Ph., and Susini, J. (2007) A multiplatform code for the analysis of energy-dispersive X-ray fluorescence spectra. Spectrochimica Acta, B 62, 63–68.

Stevens, G., Villaros, A., and Moyen, J.-F. (2007) Selective peritectic garnet entrainment as the origin of geochemical diversity in S-type granites. Geology, 35, 9–12.

Tajčmanová, L., Connolly, J.A.D, and Cesare, B. (2009) A thermodynamic model for titanium and ferric iron solution in biotite. Journal of Metamorphic Geology, 27, 153-165.

Torne, M., Fernàndez, M., Comas, M.C., and Soto., J.I. (2000) Lithospheric Structure Beneath the Alborán Basin: Results from 3D Gravity Modeling and Tectonic Relevance. Journal of Geophysical Research, 105(B2), 3209–3228, doi:10.1029/1999JB900281.

White, R.W., Powell, R. and Halpin, J.A. (2004) Spatially-focused melt formation in aluminous metapelites from Broken Hill, Australia. Journal of Metamorphic Geology, 22, 825–845.

Wolf, M.B., and Wyllie, P.J. (1991) Dehydration-melting of solid amphibolite at 10 kbar: textural development, liquid inter-connectivity and applications to the segregation of magmas. Mineralogy and Petrology, 44, 151-179.

Závada, P., K. Schulmann, J. Konopásek, S. Ulrich, and O. Lexa (2007) Extreme ductility of feldspar aggregates—Melt- enhanced grain boundary sliding and creep failure: Rheological

implications for felsic lower crust, Journal of Geophysical Research, 112, B10210, doi:10.1029/2006JB004820.

Zeck, H.P. (1970) An erupted migmatite from Cerro del Hoyazo, SE Spain. Contributions to Mineralogy and Petrology, 26, 225–246.

Zeck, H.P. (1992) Restite-melt and mafic-felsic magma mingling in an S-type dacite, Cerro del Hoyazo, southeastern Spain. Transactions of the Royal Society of Edinburgh: Earth Sciences, 83, 139–144.

Zeck H.P. and Williams, I.S. (2002) Inherited and magmatic zircon from Neogene Hoyazo cordierite dacite, SE Spain–Anatectic source rock provenance and magmatic evolution. Journal of Petrology, 43, 1089–1104.

Zhang, L., Hustache, R., Hignette, O., Ziegler, E., and Freund, A. (1998) Design optimization of a flexural hinge-based bender for X-ray optics. Journal of Synchrotron Radiation, 5, 804–807.

Whitney, D.L. and Evans, B.W. (2010) Abbreviations for names of rock-forming minerals. American Mineralogist, 95, 185–187.

FIGURE CAPTIONS

Fig. 1 – Geographical location and schematic tectonic elements of the Neogene Volcanic Province (NVP), SE Spain. a) Location map of the study area in the western Mediterranean; b) Enlargment of the area shown by the box in (a), with locations of the El Hoyazo volcanics

and main outcrops of the Neogene Volcanic Province.

Fig. 2 – (A) Field image of a typical Grt-Bt-Sil (abbreviations according to Whitney and Evans 2010) enclave within the dacitic lava of El Hoyazo, and (B) microscopic, plane-polarized light view of the sample HO1 with euhedral Grt, well-oriented Pl and Bt layers, and the Mix, a mixture of Sil + glass replacing a former Grt.

Fig. 3 – Orientation of the four sections mapped with μ-XRF: (1) HO1-YZ, (2) HO1-XZ, (3) HO1-XZexp, (4) HO1-YZdetail. The planes XY are oriented parallel to the main foliation marked by biotite and graphite. Section (4) is a selected area of section (1) mapped with high resolution (see text for details).

Fig. 4 – μ-XRF results and data processing of section (4): (A) RGB map combining the chemical signals of Si (red), K (green) and Fe (blue); (B) distribution of Bt, Mix and glass performed on the base of the Regions of Interests (ROIs) defined on RGB maps. White arrow tips point to glass films, yellow arrow tips point to glass pools; (C) chemical distribution of the element Gallium, which is characteristically present in sillimanite (grey tones, white = maximum concentration, black = minimum concentration); (D) superposition of the images B and C indicating that the glass is mostly concentrated at the outer borders of the Mix at the contact with biotite.

Fig. 5 – μ-XRF results and data processing of sections (1), (2) and (3). (A) RGB maps combining the chemical signals of Si (red), K (green) and Fe (blue); (B) distribution of Bt, Grt, Pl, Kfs, Mix and glass on the base of the Regions of Interests (ROIs) defined on RGB maps (white arrow tips=glass films, yellow arrow tips=glass pools); (C) superposition of the

phase distribution (B) and the Gallium concentration maps (not reported here). Biotite is black and glass is dark red. The grey areas correspond to Mix, Grt, Pl and Kfs.

Fig. 6 - Backscattered electron images (BSE) of glass distribution in selected areas (white arrow tips=glass films, yellow arrow tips=glass pools or intermixed glass). (A) between Pl and Grt, (B) between Pl and Bt with Spl, (C) between Bt, Grt and the Mix, (D) and (F) between Bt and the Mix, (E) in Bt aggregates (F) eventually with Grt. Detailed images of the Mix away from the contact with biotite displaying (G) pools of glass or (H) no visible glass.

Fig. 7 – Backscattered electron images (BSE) with location of EMP glass analyses reported in Table 4 (yellow arrows pointing to glass).

Fig. 8 – Harker diagrams showing the major element concentrations (wt.%) and the Aluminum Saturation Index (ASI) of the matrix melt in HO1 (Table 4) and in crustal enclaves HO-50 and PFHZ3 (Table 5 – Supplementary Material, unpublished data from Acosta-Vigil). (A) Al_2O_3 vs. SiO_2, (B) CaO vs. SiO_2, (C) ASI vs. SiO_2, (D) K_2O vs. MgO + FeOt + TiO_2.

TABLE CAPTIONS

Table 1 – Bulk composition of the enclave HO1 in weight %.

Table 2 – Representative EMP chemical analysis of minerals and glass from the enclave HO1 in weight %.

Table 3 - Modal composition of the enclave HO1 from mass balance calculation (weight

%) and from image analysis (area %) on the four thin sections.

Table 4 –- EMP analyses of matrix glass in weight % in HO1 (with indication of the mineral in proximity). Selected points are reported in Fig. 7.

Table 5 Supplementary Material - EMP analyses of matrix glass in weight % from two Grt-Bt-Sil enclaves from El Hoyazo (HO-50 and PFHz3, unpublished data from Acosta-Vigil).

This is a preprint, the final version is subject to change, of the American Mineralogist (MSA)
Cite as Authors (Year) Title. American Mineralogist, in press.
DOI: https://doi.org/10.2138/am-2018-6290

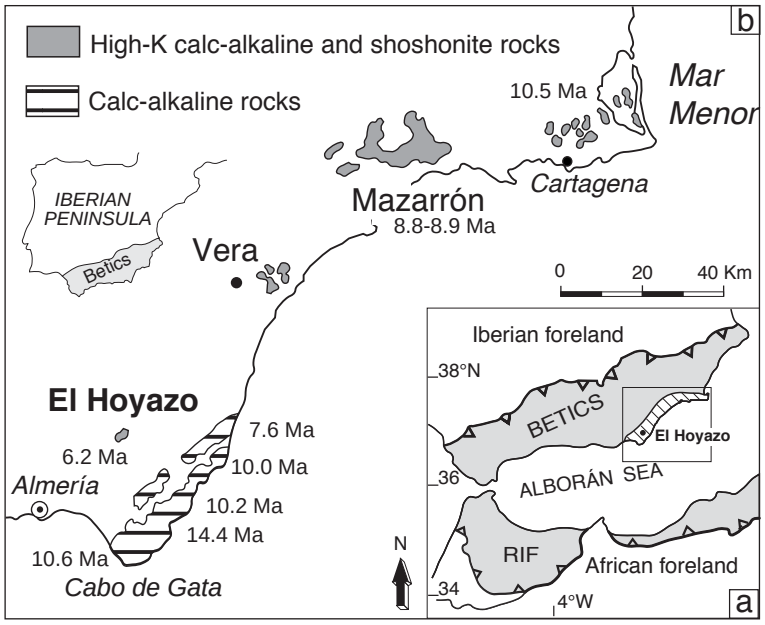

Fig. 1 - Ferri et al.

This is a preprint, the final version is subject to change, of the American Mineralogist (MSA)
Cite as Authors (Year) Title. American Mineralogist, in press.
DOI: https://doi.org/10.2138/am-2018-6290

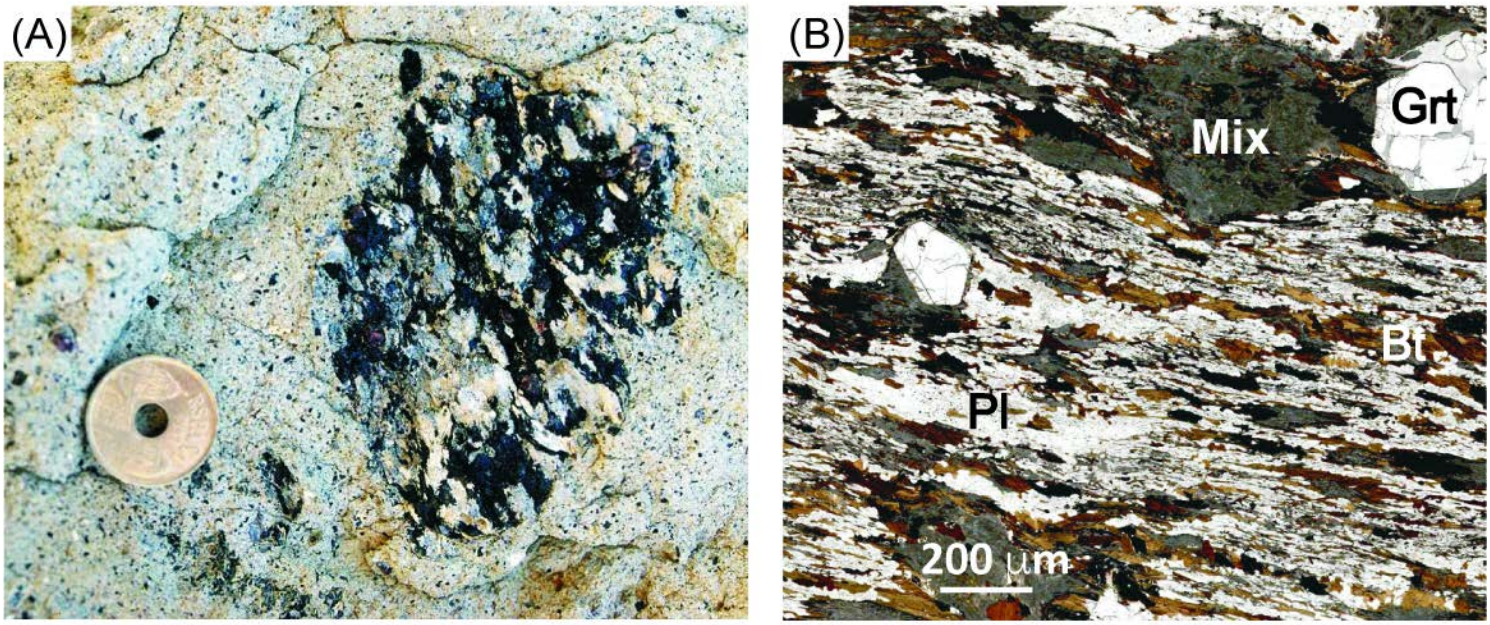

Fig. 2 - Ferri et al.

DOI: https://doi.org/10.2138/am-2018-6290

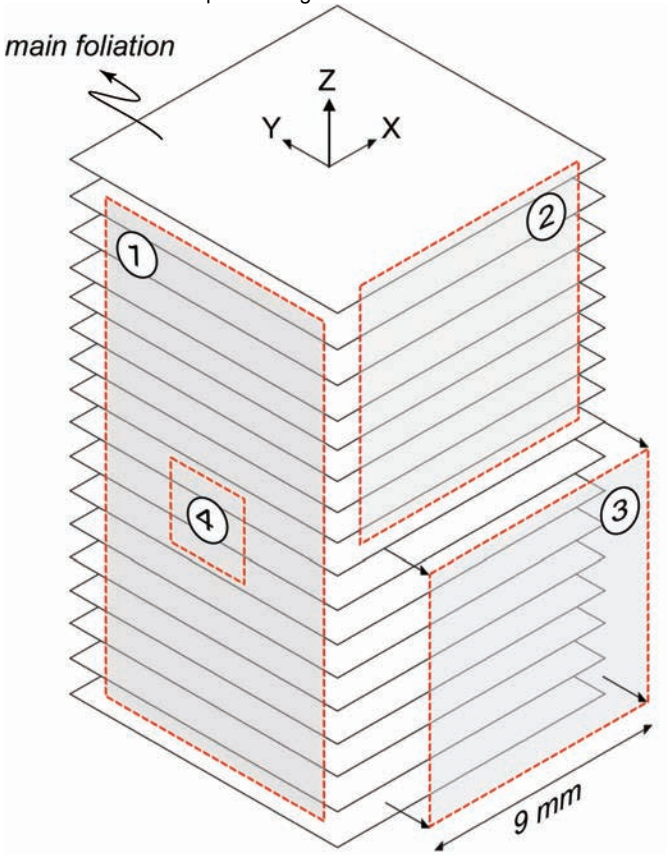

Fig. 3 - Ferri et al.

This is a preprint, the final version is subject to change, of the American Mineralogist (MSA)
Cite as Authors (Year) Title. American Mineralogist, in press.
DOI: https://doi.org/10.2138/am-2018-6290

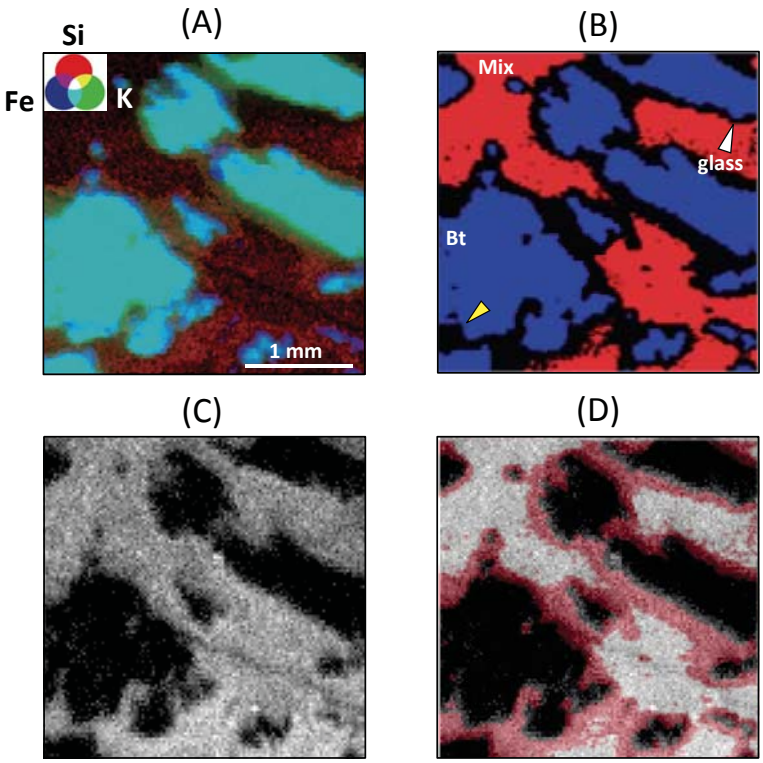

Fig. 4 - Ferri et al.

This is a preprint, the final version is subject to change, of the American Mineralogist (MSA)
Cite as Authors (Year) Title. American Mineralogist, in press.
DOI: https://doi.org/10.2138/am-2018-6290

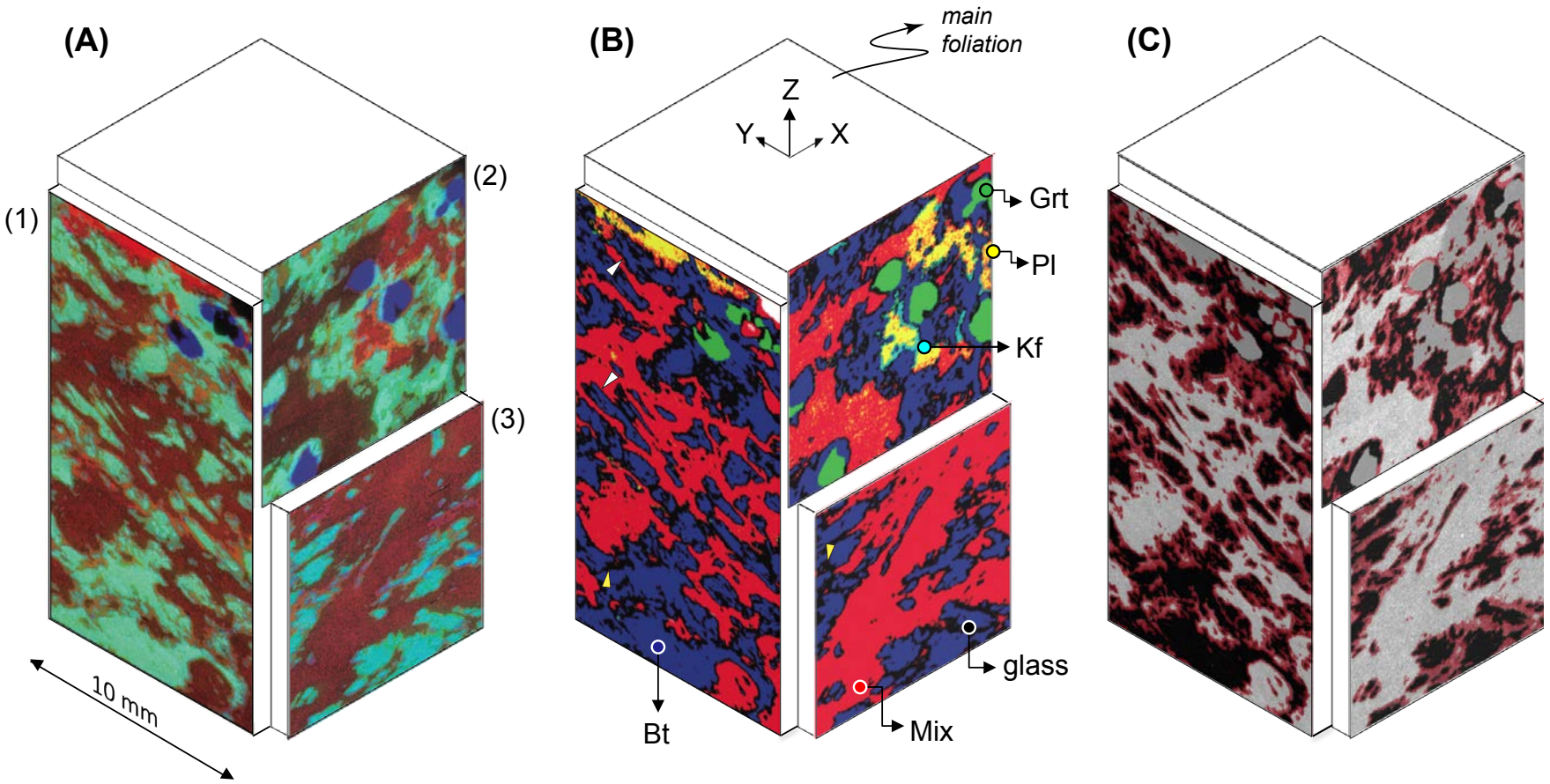

Fig. 5 - Ferri et al.

This is a preprint, the final version is subject to change, of the American Mineralogist (MSA)
Cite as Authors (Year) Title. American Mineralogist, in press.
DOI: https://doi.org/10.2138/am-2018-6290

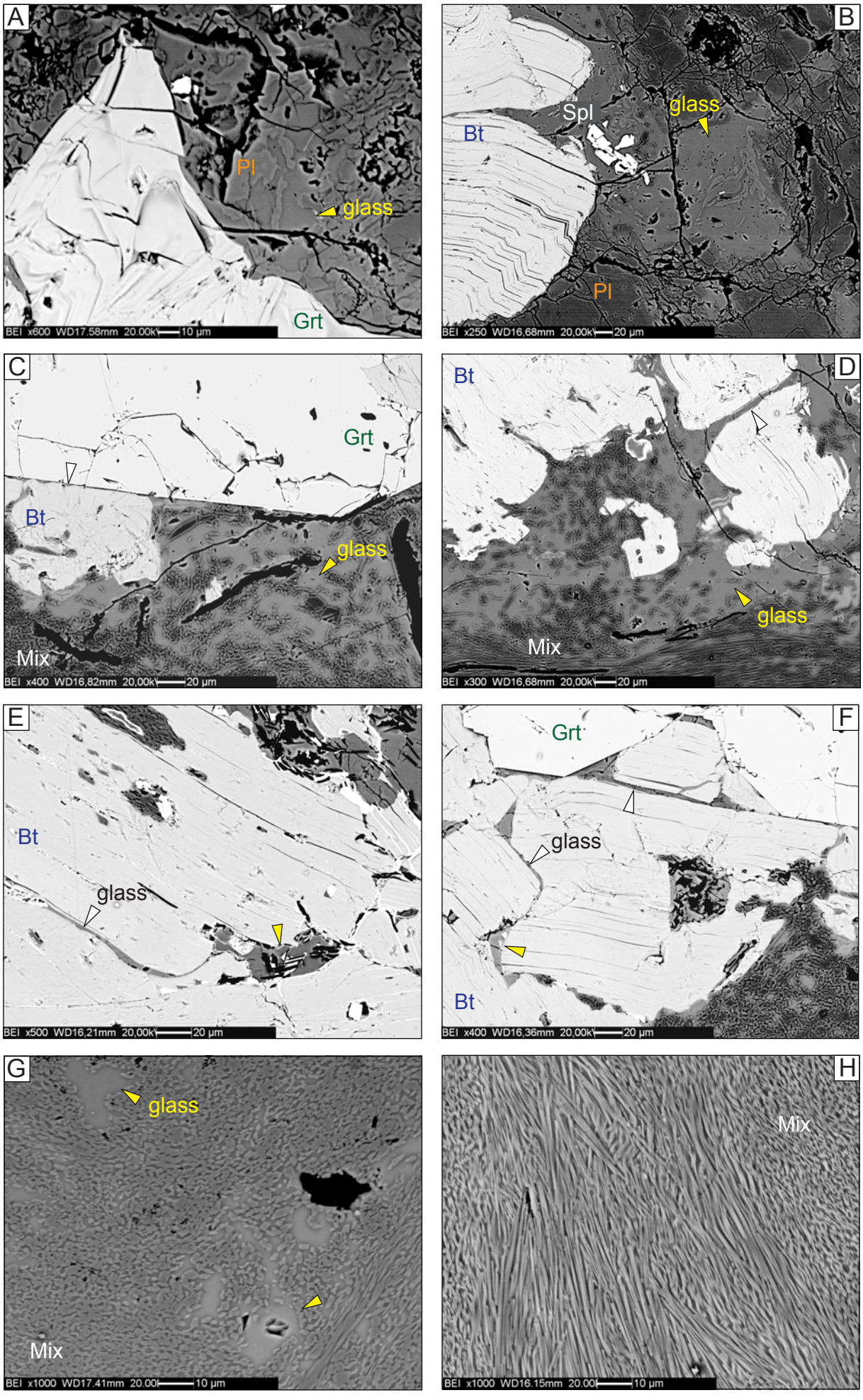

Fig. 6 - Ferri et al.

This is a preprint, the final version is subject to change, of the American Mineralogist (MSA)
Cite as Authors (Year) Title. American Mineralogist, in press.
DOI: https://doi.org/10.2138/am-2018-6290

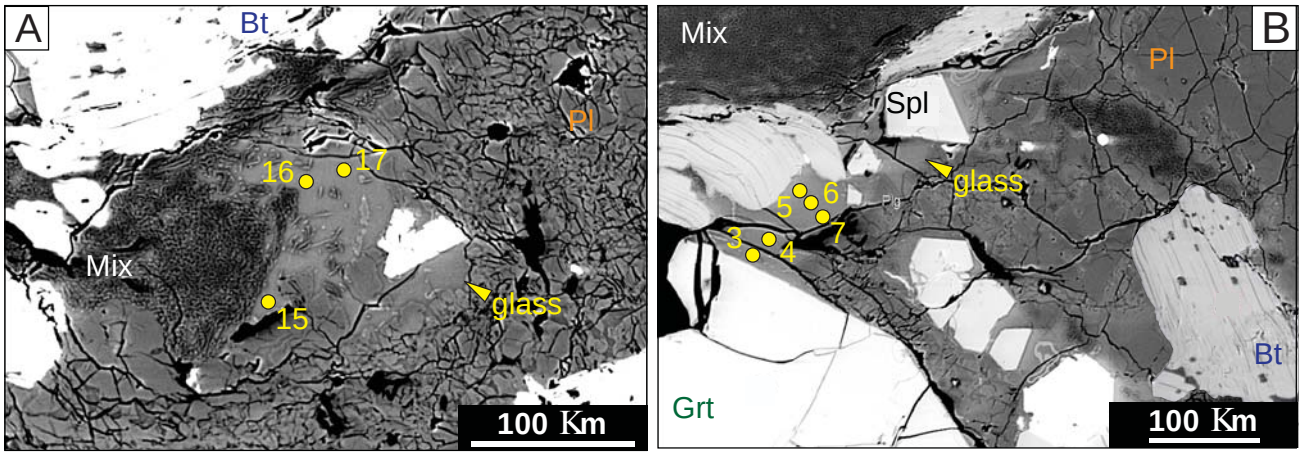

Fig. 7 - Ferri et al.

This is a preprint, the final version is subject to change, of the American Mineralogist (MSA)
Cite as Authors (Year) Title. American Mineralogist, in press.
DOI: https://doi.org/10.2138/am-2018-6290

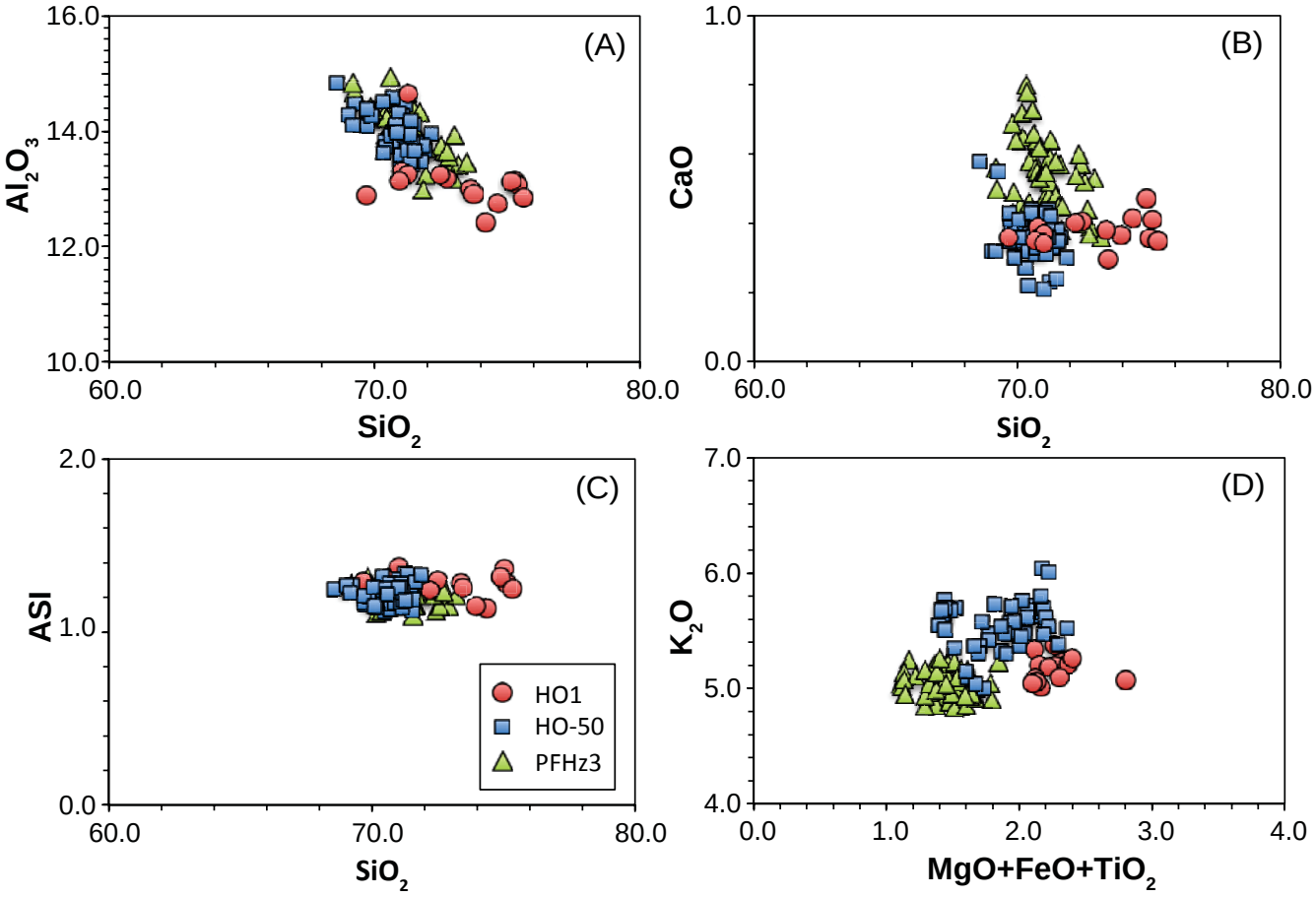

Fig. 8 - Ferri et al.

This is a preprint, the final version is subject to change, of the American Mineralogist (MSA)
Cite as Authors (Year) Title. American Mineralogist, in press.
DOI: https://doi.org/10.2138/am-2018-6290

Table 1 - Bulk composition of the enclave HO1 in weight %

	HO1
SiO_2	45.37
TiO_2	1.64
Al_2O_3	31.52
Fe_2O_{3tot}	11.04
MnO	0.10
MgO	2.55
CaO	1.65
Na_2O	1.98
K_2O	3.77
P_2O_5	0.19
L.O.I.	1.40
Total	99.81
C	0.98
Al_2O_3/SiO_2	0.69
$x_{Mg}(Fe_{tot})$	0.31

[a] L.O.I. = Loss on Ignition
[b] $x_{Mg}(Fe_{tot})=Mg/(Mg+Fe_{tot})$

This is a preprint, the final version is subject to change, of the American Mineralogist (MSA)
Cite as Authors (Year) Title. American Mineralogist, in press.
DOI: https://doi.org/10.2138/am-2018-6290

Table 2 - Representative EMP chemical analysis in weight % of minerals and glass from HO1 and represent

wt%.	Glass(Gl-3)	Biotite	Garnet	Sillimanite	K-feldspar	Plagioclase	Spinel
SiO_2	72.48	34.98	37.67	37.08	65.03	57.60	0.05
TiO_2	0.14	6.00	0.03	-	0.03	0.04	0.30
Al_2O_3	13.19	18.26	21.15	62.92	19.61	27.11	60.01
FeO	2.02	19.09	36.31	-	0.09	0.1	31.94
MnO	-	0.02	1.46	-	0.01	0.00	0.02
MgO	0.16	8.70	3.09	-	-	-	6.62
CaO	0.41	0.05	0.92	-	0.41	8.96	-
Na_2O	2.64	0.60	-	-	2.90	6.23	0.01
K_2O	5.07	8.79	0.01	-	11.60	0.81	0.01
Total	96.12	96.49	100.64	100.00	99.68	100.85	98.96

This is a preprint, the final version is subject to change, of the American Mineralogist (MSA)
Cite as Authors (Year) Title. American Mineralogist, in press.
DOI: https://doi.org/10.2138/am-2018-6290

Table 3 - Modal composition of the enclave HO1 from mass balance calculation and image analysis on the thin sections

# section		Biotite	Garnet	Sillimanite	Glass	K-feldspar	Plagioclase	Spinel	Ilmenite	epoxy	Total
		mass balance wt. %									
		22.43	15.69	23.99	8.90	10.11	16.53	2.07	0.00		99.72
		image analysis area %									
(2)	HO1-XZ	28.37	8.36	35.27	13.22	4.20	10.52	<0.4	<0.1	0.06	100.00
(3)	HO1-XZexp	21.27	-	66.32	10.89	-	-	<0.1	<0.1	1.52	100.00
(1)	HO1-YZ	29.27	2.96	42.17	14.80	-	4.20	<0.1	<0.1	6.60	100.00
(4)	HO1- YZdetail	39.31	-	47.71	12.87	-	-	<0.1	<0.2	0.11	100.00

This is a preprint, the final version is subject to change, of the American Mineralogist (MSA)
Cite as Authors (Year) Title. American Mineralogist, in press.
DOI: https://doi.org/10.2138/am-2018-6290

Table 4 - EMP analysis of matrix glass of sample HO1

Sample HO1							
Analysis ID	*Gl-4*	*Gl-5*	*Gl-6*	*Gl-7*	*Gl-8*	*Gl-9*	*Gl-10*
***adjacent mineral**	Grt-Bt	Bt	Bt-Pl	Pl	Grt	Grt	Grt
SiO_2	69.69	70.77	70.99	70.68	74.38	75.03	73.95
TiO_2	0.10	0.18	0.11	0.11	0.10	0.10	0.10
P_2O_5	0.60	0.58	0.54	0.50	0.47	0.55	0.55
Al_2O_3	12.89	13.31	13.26	13.15	12.75	13.15	12.42
FeO	2.03	1.99	1.85	2.00	2.09	2.13	1.88
MgO	0.16	0.15	0.16	0.16	0.19	0.16	0.16
CaO	0.36	0.39	0.37	0.35	0.42	0.36	0.37
Na_2O	2.48	2.57	3.07	2.46	3.17	2.29	2.94
K_2O	5.15	5.23	5.34	5.20	5.21	5.26	5.21
F	0.01	0.01	-0.01	-0.01	0.00	0.00	-0.01
Cl	0.18	0.17	0.11	0.13	0.17	0.17	0.13
O=F	0.00	0.00	0.00	0.00	0.00	0.00	0.01
O=Cl	-0.04	-0.04	-0.02	-0.03	-0.04	-0.04	-0.03
Total	93.60	95.31	95.76	94.72	98.89	99.15	97.67
$MgO+FeO+TiO_2$	2.30	2.32	2.11	2.27	2.37	2.39	2.15
ASI	1.29	1.30	1.19	1.32	1.14	1.36	1.15

*Mineral close to the analyzed glass; Grt-Bt = glass between garnet and biotite; Bt-Pl = glass b
ASI (Aluminum Saturation Index) = molar Al_2O_3/ ($CaO+Na_2O+K_2O$)

This is a preprint, the final version is subject to change, of the American Mineralogist (MSA)
Cite as Authors (Year) Title. American Mineralogist, in press.
DOI: https://doi.org/10.2138/am-2018-6290

Gl-11 Mix	*Gl-12* Mix	*Gl-13* Pl	*Gl-14* Bt-Pl	*Gl-15* Pl	*Gl-16* Pl	*Gl-17* Pl
72.20	75.12	74.88	75.34	73.36	70.99	73.46
0.14	0.11	0.11	0.13	0.10	0.10	0.09
0.54	0.50	0.48	0.51	0.58	0.51	0.57
13.25	13.09	13.14	12.86	13.01	14.66	12.92
1.91	1.84	2.02	1.97	1.87	1.85	1.84
0.17	0.17	0.18	0.16	0.19	0.17	0.17
0.40	0.41	0.47	0.35	0.38	0.34	0.30
2.87	2.72	2.56	2.61	2.66	2.96	2.77
5.18	5.09	5.10	5.38	5.01	5.06	5.04
-0.01	-0.02	0.03	-0.01	-0.01	0.00	0.00
0.14	0.14	0.17	0.18	0.14	0.16	0.13
0.00	0.01	-0.01	0.00	0.00	0.00	0.00
-0.03	-0.03	-0.04	-0.04	-0.03	-0.04	-0.03
96.77	99.15	99.08	99.45	97.25	96.77	97.25
2.22	2.12	2.30	2.26	2.16	2.13	2.10
1.24	1.28	1.32	1.25	1.29	1.38	1.26

›etween biotite and plagioclase.